



UPPSALA
UNIVERSITET

*Digital Comprehensive Summaries of Uppsala Dissertations
from the Faculty of Science and Technology 1584*

Energy Storage Materials: Insights From *ab Initio* Theory

Diffusion, Structure, Thermodynamics and Design.

RAFAEL BARROS NEVES DE ARAÚJO



ACTA
UNIVERSITATIS
UPSALIENSIS
UPPSALA
2017

ISSN 1651-6214
ISBN 978-91-513-0122-8
urn:nbn:se:uu:diva-331399

Dissertation presented at Uppsala University to be publicly examined in Polhemsalen, Ångström Laboratory, Lägerhyddsvägen 1, Uppsala, Thursday, 7 December 2017 at 13:15 for the degree of Doctor of Philosophy. The examination will be conducted in English. Faculty examiner: Professor Graeme Henkelman (University of Texas at Austin).

Abstract

Araújo, R. B. N. d. 2017. Energy Storage Materials: Insights From *ab Initio* Theory. *Diffusion, Structure, Thermodynamics and Design.. Digital Comprehensive Summaries of Uppsala Dissertations from the Faculty of Science and Technology* 1584. 83 pp. Uppsala: Acta Universitatis Upsaliensis. ISBN 978-91-513-0122-8.

The development of science and technology have provided a lifestyle completely dependent on energy consumption. Devices such as computers and mobile phones are good examples of how our daily life depends on electric energy. In this scenario, energy storage technologies emerge with strategic importance providing efficient ways to transport and commercialize the produced energy. Rechargeable batteries come as the most suitable alternative to fulfill the market demand due to their higher energy- and power- density when compared with other electrochemical energy storage systems. In this context, during the production of this thesis, promising compounds for advanced batteries application were investigated from the theoretical viewpoint. The framework of the density functional theory has been employed together with others theoretical tools to study properties such as ionic diffusion, redox potential, electronic structure and crystal structure prediction.

Different organic materials were theoretically characterized with quite distinct objectives. For instance, a protocol able to predict the redox potential in solution of long oligomers were developed and tested against experimental measurements. Strategies such as anchoring of small active molecules on polymers backbone have also been investigated through a screening process that determined the most promising candidates. Methods such as evolutionary simulation and basin-hopping algorithm were employed to search for global minimum crystal structures of small molecules and inorganic compounds working as a cathode of advanced sodium batteries. The crystal structure evolution of $\text{C}_6\text{Cl}_4\text{O}_2$ upon Na insertion was unveiled and the main reasons behind the lower specific capacity obtained in the experiment were clarified. *Ab initio* molecular dynamics and the nudged elastic band method were employed to understand the underlying ionic diffusion mechanisms in the recently proposed Alluaudite and Eldfellite cathode materials. Moreover, it was demonstrated that electronic conduction in Na_2O_2 , a byproduct of the Na- O_2 battery, occurs via hole polarons hopping. Important physical and chemical insights were obtained during the production of this thesis. It finally supports the development of low production cost, environmental friendliness and efficient electrode compounds for advanced secondary batteries.

Keywords: Density Functional Theory, Defects Diffusion, Thermodynamics and Batteries.

Rafael Barros Neves de Araújo, Department of Physics and Astronomy, Materials Theory, Box 516, Uppsala University, SE-751 20 Uppsala, Sweden.

© Rafael Barros Neves de Araújo 2017

ISSN 1651-6214

ISBN 978-91-513-0122-8

urn:nbn:se:uu:diva-331399 (<http://urn.kb.se/resolve?urn=urn:nbn:se:uu:diva-331399>)

Dedicated to all my family and my lovely wife

List of Papers

This thesis is based on the following papers, which are referred to in the text by their Roman numerals.

- I **Unveiling the charge migration mechanism in Na_2O_2 : implications for sodium air batteries**
R. B. Araujo, S. Chakraborty and R. Ahuja
Phys. Chem. Chem. Phys., 2015, 17, 8203
- II **Predicting electrochemical properties and ionic diffusion in $\text{Na}_{2+2x}\text{Mn}_{2-x}(\text{SO}_4)_3$: crafting a promising high voltage cathode material**
R. B. Araujo, M. S. Islam, S. Chakraborty and R. Ahuja
J. Mater. Chem. A, 2016, 4, 451-457
- III **Designing strategies to tune reduction potential of organic molecules for sustainable high capacity batteries application**
R. B. Araujo, A. Banerjee, P. Panigrahi, L. Yang, M. Strømme, M. Sjödín, C. M. Araujo and R. Ahuja
J. Mater. Chem. A, 2017, 5, 4430-4454
- IV **Divulging the Hidden Capacity and Sodiation Kinetics of $\text{Na}_x\text{C}_6\text{Cl}_4\text{O}_2$: A High Voltage Organic**
R. B. Araujo, A. Banerjee and R. Ahuja
J. Chem. C., 2017, 121, 14027
- V **$\text{Na}_{2.44}\text{Mn}_{1.79}(\text{SO}_4)_3$: A new member of alluaudite family of insertion compounds for sodium ion batteries**
D. Dwivedi, **R. B. Araujo**, S. Chakraborty, P. P. Shanbogh, N. G. Sundaram, R. Ahuja, and P. Barpanda
J. Mater. Chem. A, 2015, 3, 18564-18571
- VI **$\text{Na}_2\text{M}_2(\text{SO}_4)_3$ (M=Fe, Mn, Co and Ni): Towards High Voltage Sodium Battery Applications**
R. B. Araujo, S. Chakraborty, P. Barpanda and R. Ahuja
Phys. Chem. Chem. Phys., 2016, 18(14), 9658-9665
- VII **Evaluating bulk $\text{Nb}_2\text{O}_5\text{F}_3$ for Li-battery electrode application**
R. B. Araujo and R. Ahuja
Phys. Chem. Chem. Phys., 2016, 18(5), 3530-5.

- VIII **First-principles investigation of Li ion diffusion in $\text{Li}_2\text{FeSiO}_4$**
R. B. Araujo, J . S. de Almeida, R. H. Scheicher, A. F. da Silva and R. Ahuja
Solid State Ionics, 2013, 247, 8-14
- IX **Lithium transport investigation in $\text{Li}_x\text{FeSiO}_4$: A promising cathode material**
R. B. Araujo, J . S. de Almeida, R. H. Scheicher, A. F. da Silva and R. Ahuja
Solid State Communications, 2013, 173, 9-13
- X **Assessing Electrochemical Properties of Polypyridine and Polythiophene for Prospective Application in Sustainable Organic Batteries**
R. B Araujo, A. Banerjee, P. Panigrahi, L. Yang, M. Sjödin, M. Strømme, C. M. Araujo and R. Ahuja
Phys. Chem. Chem. Phys, 2017, 19, 3307-3314
- XI **Unveiling the Thermodynamic and Kinetic Properties of $\text{Na}_x\text{Fe}(\text{SO}_4)_2$ ($x=0-2$): Toward a High-capacity and Low-cost Cathode Material**
A. Banerjee, **R. B. Araujo** and R. Ahuja
J.I Mater. Chem. A, 2016, 4, 17960-17969
- XII **The Curious Case of Two Dimensional Si_2BN : A High-capacity Battery Anode Material**
V. Shukla, **R. B. Araujo**, N. K. Jena and R. Ahuja
Nano Energy, 2017
- XIII **Borophane as a Benchmate of Graphene: A Potential 2D Material for Anode of Li and Na-Ion Batteries**
Naresh K. Jena, **Rafael B. Araujo**, Vivekanand Shukla and Rajeev Ahuja
ACS Appl. Mater. Interfaces, 2017, 9, 16148-16158
- XIV **Ionothermal Synthesis of High-Voltage Alluaudite $\text{Na}_{2+2x}\text{Fe}_{2-x}(\text{SO}_4)_3$ Sodium Insertion Compound: Structural, Electronic, and Magnetic Insights**
D. Dwivedi, C. D. Ling, **R. B. Araujo**, S. Chakraborty, S. Duraisamy, N. Munichandraiah, R. Ahuja and P. Barpanda
ACS Appl. Mater. Interfaces, 2016, 8, 6982
- XV **$\text{Na}_{2.32}\text{Co}_{1.84}(\text{SO}_4)_3$ as a New Member of Alluaudite Family of High-Voltage Sodium Battery Cathode**
D. Dwivedi, R. Gond, A. Dayamani, **R. B. Araujo**, S. Chakraborty, R. Ahuja and P. Barpanda

Dalton Trans., 2017, 46, 55-63

XVI Probing the pseudo-1-D ion diffusion in lithium titanium niobate anode for Li-ion battery

S. Das, D. Dutta, **R. B. Araujo**, S. Chakraborty, R. Ahuja and A. J. Bhattacharyya

Phys. Chem. Chem. Phys., 2016, 18, 22323-22330

Reprints were made with permission from the publishers.

List of Papers not Included in the Thesis

During this thesis the following works were also made, but are not included in the thesis.

- I **Electronic properties of III-nitride semiconductors: A first-principles investigation using the Tran-Blaha modified Becke-Johnson potential**
R. B. Araujo, J. S. de Almeida and A. F. da Silva
J. Appl. Phys., 2013, 114 (18), 1837027
- II **Photocatalytic hydrogen production with visible light over Mo and Cr-doped BiNb(Ta)O₄**
C. G. Almeida, **R. B. Araujo**, R. G. Yoshimura, A. J. S. Mascarenhas, A. F. da Silva, C. M. Araujo and L. A. Silva
International journal of hydrogen energy, 2014, 39 (3), 1220-1227
- III **Insights in the electronic structure and redox reaction energy in LiFePO₄ battery material from an accurate Tran-Blaha modified Becke Johnson potential**
R. B. Araujo, J. S. de Almeida, A. F. da Silva and R. Ahuja
J. Appl. Phys., 2015, 118, 125107
- IV **Alloying in an intercalation host: An alternative chemical design strategy of anodes for rechargeable alkali-ion batteries**
S. Das, **R. B. Araujo**, S. Songxin, R. Ahuja and A. J. Bhattacharyya
Submitted to Chemistry of Materials
- V **Current Computational Trends in Polyanionic Cathode Materials for Li and Na Batteries**
S. Chakraborty, A. Banerjee, T. Watcharatharapong, **R. B. Araujo** and R. Ahuja
Manuscript
- VI **Identifying the Tuning Key of Disproportionation Redox Reaction in Terephthalate: A Li-based Anode for Sustainable Organic Batteries**
A. Banerjee, **R. B. Araujo**, M. Sjödín and R. Ahuja
Manuscript

Comments on my contributions

Papers I, II, III, IV, VI, VII, VIII, IX and X:

I have participated in the designing of the research, performed the calculations and analyzed data. I took responsibility to write the first manuscript and contributed during the writing process.

Papers XI, XII and XIII:

I have participated in the designing of the research, performed part of the calculations and analyzed data. I also have contributed to the writing process.

Papers V, XIV, X and XI:

I have designed and performed the theoretical calculations and analyzed the data (coming from the calculations). I also wrote the first draft of the theoretical contributions of these papers and contributed during the writing process. I have not participated in the performed experiments.

Contents

1	Introduction	13
1.1	Some Concepts of the Battery Performance	16
2	Density Functional Theory	17
2.1	The Many-Body Problem	17
2.2	Born-Oppenheimer Approximation	18
2.3	The Hohenberg-Kohn Theorems	18
2.4	Kohn-Sham Ansatz	19
2.5	Exchange and Correlation Functional	20
2.5.1	Self-Interaction Error	21
2.5.2	DFT+U Approach	22
2.5.3	Hybrid Functional	22
2.5.4	Van der Waals Interactions	23
2.6	Computational Methods	24
2.6.1	Basis Set	24
2.6.2	Bloch Electrons	25
2.6.3	PAW Method	25
2.7	Force Theorem	27
3	Ionic Diffusion	29
3.1	Molecular Dynamics	29
3.2	Transition State Theory	30
3.3	Finding the Saddle Point	33
3.4	Case 01: Ionic Migration in $\text{Li}_2\text{FeSiO}_4$	34
3.4.1	The Effects of the U Term in the Activation Energy	35
3.4.2	Monoclinic vs. Orthorhombic Structures	36
3.5	Case 02: Na Diffusion in $\text{Na}_{2.5}\text{Mn}_{1.75}(\text{SO}_4)_3$	36
3.6	Case 03: Ionic Diffusion in $\text{Na}_x\text{Fe}(\text{SO}_4)_2$	38
3.7	Case 04: Polaron Migration Mechanism in Na_2O_2	40
4	Thermodynamics of Ions Insertion	45
4.1	Equilibrium Crystal Structure Prediction	46
4.1.1	Basin-hopping	46
4.1.2	Evolutionary Algorithm	47
4.2	Case 01: Ionic Insertion in $\text{Na}_x\text{Fe}(\text{SO}_4)_2$	48
4.3	Case 02: $\text{C}_6\text{Cl}_4\text{O}_2$ as an Organic Cathode of Sodium Batteries ..	50
4.3.1	The Crystal Structure Search	51

4.3.2	The Ionic Insertion Potential and Capacity	52
4.4	Case 03: 2D compounds as the anode of rechargeable batteries	54
4.4.1	The 2D-B ₂ H ₂ anode	55
4.4.2	The 2D-Si ₂ BN anode	57
5	Electronic Structure and Charge Disproportionation Analysis	59
5.1	Case 01: Nb ₂ O ₂ F ₃	59
5.2	Case 02: Na ₂ M ₂ (SO ₄) ₃ with M=Fe, Mn, Co and Ni	61
6	Theory to Predict Redox Potential in Solution	63
6.1	Organic Compounds as the Electrode of Rechargeable Batteries	65
6.2	Case 01: Assessing Electrochemical Properties of conjugated polymers	65
6.3	Case 02: Designing Strategies to Tune Reduction Potential of Organic Molecules	68
7	Summary	72
8	Sammanfattning	74
9	Acknowledgments	76
	References	77

1. Introduction

Recently, the high development of science and technology has provided a lifestyle completely dependent on energy consumption. Devices such as computers and mobile phones are good examples of how our daily life depends mainly on electric energy. However, there is no guaranty that the rate of energy production will follow the rate of energy consumption in a long range future. This statement is based on the fact that part of the energy matrix used nowadays comes from non-renewable sources such as fossil fuels. Moreover, the combustion of fossil fuels releases CO_2 into the atmosphere raising the world's global warming. Some estimations of the International Energy Agency (IEA) claim that the world's energy demand will increase from 12 billion tonne oil equivalent in 2009 to over 18 billion tonne equivalent (t.o.e) in 2035 [1, 2]. Carbon dioxide emission would undergo a rapid growth from 29 gigatonnes per year to, in the best possibility, 36 gigatonnes per year [1, 2]. With this scenario, the scientific community has been spending a great effort to come up with good alternatives for the currently used of energy sources. The main goal is to promote an easy transition to one energy matrix that is renewable, environmentally friendly and cheap enough to compete with fossil fuels [2]. Then, totally replacing the current fossil fuel economy by one that is sustainable in the long term.

Energy storage technologies will play an important role in this new energetic scenario providing efficient ways to transport and commercialize the energy produced by renewable technologies such as wind or solar power [2]. Li-ion batteries appear as one of the most suitable alternatives to help in this transition of energetic matrix owed to their high energy- and power-densities compared with the currently used electrochemical storage devices [3] quickly dominating the market of portable electronics, for instance.

The first commercialized Li battery dates back to 1991 [4]. In this cell, a cathode formed of LiCoO_2 and a graphite anode were employed as a result of investigations performed by Goodenough et al. [5] and Yazami et al. [6]. The first reaction step of the mentioned electrochemical device (charge procedure) is the extraction of Li ions from the positive electrode (oxidation) and intercalate them into the negative electrode, formed of graphite layers (reduction). During this procedure, Li^+ ions move through the electrolyte and electrons are released to an external circuit migrating from the positive electrode to the negative electrode and ensuring the electrical neutrality of the compounds. Then, the cell can be discharged through the opposite redox reaction and, the accumulated energy can be used in some external device. Figure 1.1 represents the charge and discharge process of a Li rechargeable battery.

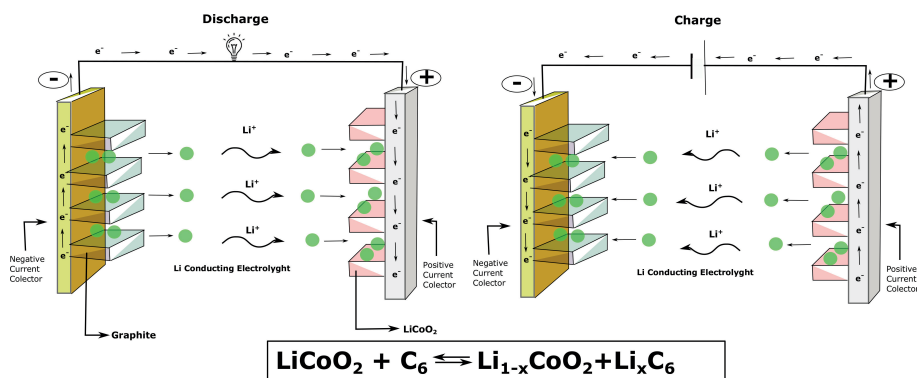


Figure 1.1. Schematic picture showing the operating principle of a rechargeable Li battery

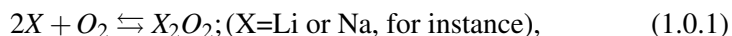
Even considering the great success of this sort of devices, it still presents some disadvantages. State-of-art lithium batteries accounts for lower specific energy in comparison to power sources such as gasoline. It results in general difficulties for the application of rechargeable batteries in systems such as all-electric vehicles [7], for instance. When one refers to applications where the delivered gravimetric energy is not a concern, such as power grids, the application of Li based technologies emerges with a disadvantage as well. This is owed to the high cost of production of Li increasing the final price of the device. Therefore, these emerging markets where the application of well established Li storage systems display issues have spurred investigations for new storage systems presenting higher specific energy combined with a low cost of production and environmentally friendly.

The application of organic compounds as the electrode of rechargeable batteries, for example, emerges as a possibility for the next generation of large scale energy storage devices. This is due to their abundant source, environmentally friendly, design flexibility and versatile functions [8]. The use of organic electrodes is not a new concept and dates back to 1960's when William et al. [9] have used dichloroisocyanuric acid as the cathode of a non-rechargeable cell. They obtained two discharge plateaus displaying 3.5 V vs. Li/Li^+ and 3.0 V vs. Li/Li^+ during the discharge reaction. However, due to the formation of inactive precipitates, the reversible reaction was not possible. Following the concept, Alt et al. [10] have studied carbonyl compounds at the beginning of the 1970's. Since then, the application of organic compounds as electrodes has sporadically been studied due to the great performance of inorganic electrodes such as LiCoO_2 . Only in the latest years, the scientific community has paid attention for such materials. The main drawbacks in the application of organic materials are associated with poor electrical conductivity, high solubility

in the commonly used electrolytes, low energy densities due to the low delivered potentials and limited cycle life. Nowadays, the investigations concerning organic materials for batteries are focused mainly in three groups: organosulfur compounds, free radical compounds and carbonyl compounds [11]. From these groups, carbonyl compounds have been extensively studied since the reports of Chen et al. [12, 13] proposing LiC_6O_6 as a potential candidate as an anode of Li batteries.

The application of the Li chemistry in large storage energy devices yields a great production cost. This is due to the high demand of lithium coming from different applications such as Li-batteries, manufacturing of glasses, ceramic, pharmaceuticals etc. These ensure a limited lithium resource leading to high prices. Hence, a great alternative it is to substitute the currently used Li chemistry for a Na based technology. Sodium is a cheaper compound in comparison to Li and it is well spread around the earth crust. However, despite the vigorous effort of the scientific community to produce competitive sodium based batteries, there are still some limitations that need to be addressed. Among them is the lower theoretical voltage in comparison to Li systems, the limited alternatives of host compounds and also the large volume expansions experienced by the host during the cell reaction. Significant progress has been reached recently and, in a near future, it is expected that Na-based technologies find their maturity solving most of these problems.

One possibility going beyond Li-ion technologies includes the so called metal-air batteries wherein Li-O_2 and Na-O_2 are the most known examples. These systems can reach specific energies as high as 3505 Wh/g for the lithium case and 1605 Wh/g for the sodium case [7, 14, 15]. During the discharge of these batteries, the metal coming from the anode reacts with oxygen from the air precipitating on top of a porous electrode. The basic reaction happening in the air cell can be expressed as:



Where the dominant discharge product forms Li_2O_2 for the lithium case. LiO_2 , Li_2O or even amorphous Li_2O_2 are also observed as the byproduct of the battery reaction. From side reactions, the formation of lithium carbonate, lithium acetate or even lithium fluoride [16, 17] can exist. In the case where sodium is the alkaline metal the main discharge products observed are sodium peroxide, Na_2O_2 , and sodium superoxide, NaO_2 [15]. During the recharge, an applied potential decomposes the formed oxides releasing Li or Na to the negative electrode and oxygen to the air.

Even considering metal air batteries as promising candidates to the next generation of energy storage devices, many issues have to be addressed in these systems. Some of them are: charge transport in the discharge product [18–21], oxygen transport in the electrolyte [22], degradation process [23].

1.1 Some Concepts of the Battery Performance

1. The first important concept, applied many times during this thesis, is the electrochemical cell voltage U . This is a measure of the chemical potential difference experimented by the ions in the anode and cathode. Chapter 4, properly display how to obtain this quantity through the computational framework. This voltage is also referred as OCV (open circuit voltage) when there are no electrons flowing in the cell.
2. The second concept is the battery theoretical specific capacity. It is a measure of how much charge can be stored per unit of weight of active material. Usually, this quantity is computed as:

$$C = \frac{nF}{3.6 \times MW} \quad (1.1.1)$$

where C is the capacity, n is the number of electrons participating in the reaction, MW is the molecular weight and F stands for the Faraday constant. Sometimes, the concept of volumetric capacity can also be used when the capacity is expressed per unit of volume of the active material.

3. The specific energy is defined as the maximum amount of energy stored per unit of weight (Wh/g). The volumetric energy concerns the energy stored per unit of volume (Wh/dm³).
4. The specific power comes as a quantity to measure the rate that energy can be delivered. It is defined as the energy per time unit and Kg. The power of the battery is balanced by the kinetics of the redox reaction being dependent on ionic and electronic conductivity.
5. Cycle life is the number of times that an electrochemical cell can be charged and discharged before the capacity reaches a limit. Usually, this limit is set to 80 % of the initial value.

2. Density Functional Theory

The solution of the time independent Schrödinger equation emerges as the main goal to investigate multi-electronic systems such as molecules and solids.

$$H\Psi(\mathbf{r}_1, \mathbf{r}_2, \dots, \mathbf{r}_N) = E\Psi(\mathbf{r}_1, \mathbf{r}_2, \dots, \mathbf{r}_N) \quad (2.0.1)$$

This is surely a complex task where the main issue comes from the exhibited interaction among electrons resulting in a correlated electronic motion. The density functional theory (DFT) rises as one of the most successful and used methods to treat the many-electrons problem. The framework of the DFT is based on the Hohenberg-Kohn theorems [24] where the electronic density is the main entity to describe or model such systems. In the past years, the DFT has been applied to many areas of investigation owed to its high efficiency and accuracy to compute electronic structures.

2.1 The Many-Body Problem

The first step to solve the Schrödinger equation of a many-electrons body is to create a representative Hamiltonian of n interacting electrons and t nuclei. This Hamiltonian can be written as:

$$H_t = - \underbrace{\sum_i \frac{\hbar^2}{2m_i} \nabla_i^2}_{T_e} - \underbrace{\sum_I \frac{\hbar^2}{2M_I} \nabla_I^2}_{T_N} + \underbrace{\frac{1}{2} \sum_{i \neq j} \frac{e^2}{|\mathbf{r}_i - \mathbf{r}_j|}}_{V_{ee}} - \underbrace{\sum_{i \neq I} \frac{Z_I e^2}{|\mathbf{r}_i - \mathbf{R}_I|}}_{V_{eN}} + \underbrace{\frac{1}{2} \sum_{I \neq J} \frac{Z_I Z_J e^2}{|\mathbf{R}_I - \mathbf{R}_J|}}_{V_{NN}} \quad (2.1.1)$$

where M_I is the mass of the nucleus at position \mathbf{R} , m_i is the electron mass at position \mathbf{r} and Z is the atomic number. The first and second terms of eq. 2.1.1 describe the kinetic energy of electrons and nuclei, respectively. V_{ee} , V_{eN} , V_{NN} represent the electron-electron, electrons-nuclei and nuclei-nuclei interactions. However, the solution of the Schrödinger equation with the respective Hamiltonian becomes accessible only for the hydrogen atom. Even in the case of helium, it is necessary to use approximations. For solids or more complex molecules, it turns the problem even harder due to the high complexity of the interacting electrons and nuclei. Hence, a few approximations become vital to finally resolve these issues. The first approximation is named Born-Oppenheimer.

2.2 Born–Oppenheimer Approximation

The primary objective of the Born–Oppenheimer approximation is to factorize the total wave function in two independent parts, the electronic and nuclear. This practice is justified by the heavier mass displayed by the nuclei in comparison to the electrons mass. Then, it is reasonable to consider that the dynamics of the electrons occurs in instantaneous equilibrium in respect to the nuclei movement. This consideration allows the separation of eq. 2.1.1 as the sum of the electronic Hamiltonian plus the nuclei Hamiltonian, as:

$$H_t = H_e + H_n, \quad (2.2.1)$$

where the electronic part, H_e , refers to the first, third and fourth terms of eq. 2.1.1. H_n , the nuclei part, refers to the second and fifth terms.

The total wave function is read as,

$$\Theta(\mathbf{r}, \mathbf{R}) = \chi(\mathbf{R})\Psi(\mathbf{r}, \mathbf{R}), \quad (2.2.2)$$

where χ is the nuclei wave function and Ψ is the electronic wave function. This approach allows the redefinition of the Schrödinger equation with two main parts:

$$[T_e + V_{ee}(\mathbf{r}) + V_{eN}(\mathbf{r}, \mathbf{R})]\Psi(\mathbf{r}, \mathbf{R}) = \varepsilon(\mathbf{R})\Psi(\mathbf{r}, \mathbf{R}) \quad (2.2.3)$$

$$[T_N + V_{NN}(\mathbf{R}) + \varepsilon(\mathbf{R})]\chi(\mathbf{R}) = E\chi(\mathbf{R}) \quad (2.2.4)$$

where eq. 2.2.3 is the electronic eigenvalue equation which the solution produces a set of eigenvalues and wave functions parameterized by the nuclear positions. For each solution of eq. 2.2.3 a new solution of eq. 2.2.4 is possible. This procedure creates an electronic surface denominated Born–Oppenheimer surface.

2.3 The Hohenberg–Kohn Theorems

The Hohenberg–Kohn theorems [24] arise as the basis of the density functional theory. Their formalism, based on the electronic density as the main entity to describe a physical system, permits the exact solution of the electronic problem. The corresponding theorems are:

Theorem 01: For any problem of interacting particles in an external potential $V_{\text{ext}}(\mathbf{r})$, exist an one-to-one correspondence, except for a constant, between this potential and the ground state electronic density $\rho_0(\mathbf{r})$.

In other words, this theorem states that the electronic density contains all the necessary information to correctly describe any physical system. Then, it

is possible to write a physical observable A as a functional of the ground state electronic density.

$$\langle \Psi | A | \Psi \rangle = A[\rho(\mathbf{r})] \quad (2.3.1)$$

Theorem 02: For any applied external potential in an interacting many-body system, the total energy can be written as a functional of the density. Then, the exact electronic density is the one that minimizes the total energy functional.

Based on the aforementioned theorems, the expectation value of the electronic Hamiltonian can be read as:

$$E[\rho(\mathbf{r})] = \langle \Psi | H | \Psi \rangle \quad (2.3.2)$$

where $E[\rho(\mathbf{r})]$ is the energy functional.

Therefore, the ground state of a physical system is the one in which the electronic density minimizes eq. 2.3.2 as

$$\frac{\delta}{\delta \rho} E[\rho(\mathbf{r})] \big|_{\rho=\rho_0} = 0 \quad (2.3.3)$$

with

$$E_0 = E[\rho_0(\mathbf{r})]. \quad (2.3.4)$$

2.4 Kohn–Sham Ansatz

The fundamental idea behind the Kohn–Sham ansatz [25] is to assume that the ground state electronic density of an interacting many-body system is the same as an artificial non-interacting system in an applied effective external potential. In this way the energy functional can be expressed as:

$$E_0[\rho(\mathbf{r})] = T[\rho(\mathbf{r})] + \int V_{ext}(\mathbf{r})\rho(\mathbf{r})d\mathbf{r} + \frac{1}{2} \iint \frac{\rho(\mathbf{r})\rho(\mathbf{r}')}{|\mathbf{r}-\mathbf{r}'|} d\mathbf{r}d\mathbf{r}' + E_{xc}[\rho(\mathbf{r})], \quad (2.4.1)$$

Where, $E_{xc} = E_x[\rho(\mathbf{r})] + E_c[\rho(\mathbf{r})]$, is the exchange and correlation term, $T[\rho(\mathbf{r})]$ is the kinetic energy of a non-interacting electron gas, $\frac{1}{2} \iint \frac{\rho(\mathbf{r})\rho(\mathbf{r}')}{|\mathbf{r}-\mathbf{r}'|} d\mathbf{r}d\mathbf{r}'$, is the Hartree energy and, V_{ext} , is the external potential coming from the nuclei. Here, the exchange and correlation functional covers all the many-body effects lost with the assumption of a non-interaction electronic system. An explicit form of this functional is, in fact, unknown. Hence, for practical applications,

approximations of this term have to be considered. We will discuss on this topic in the next section.

Following the second theorem, the minimization of the energy functional, eq. 2.4.1, with the constraint of the conserved particle number, leads to the so called single particle Kohn–Sham equation 2.4.2,

$$\left[-\frac{\hbar^2}{2m} \nabla^2 + V_{eff}(\mathbf{r}) \right] \psi_i(\mathbf{r}) = \varepsilon_i \psi_i(\mathbf{r}) \quad (2.4.2)$$

with

$$V_{eff}(\mathbf{r}) = V_{ext}(\mathbf{r}) + V_H(\mathbf{r}) + V_{xc}(\mathbf{r}), \quad (2.4.3)$$

$$V_{xc} = \frac{\delta E_{xc}[\rho(\mathbf{r})]}{\delta \rho(\mathbf{r})} \quad (2.4.4)$$

where the charge density can be written as

$$\rho(\mathbf{r}) = \sum_{i=1}^N |\psi_i(\mathbf{r})|^2, \quad (2.4.5)$$

with these equations solved interactively in a self-consistent process up to a required accuracy, one can obtain the electronic ground state energy.

If we assume that the exchange and correlation functional is known, then, an exact solution of the many-body problem can be found. However, in practical applications, the choice of the functional is entirely related to the accuracy of the obtained results making it one of the most important variables to properly describe any physical or chemical property.

2.5 Exchange and Correlation Functional

The exchange and correlation term, into the Kohn-Sham formalism, is interpreted as the difference between the real system (interacting system) and the artificial non-interact system. This term of the Kohn-Sham Hamiltonian can not be explicitly computed to general systems, unless for the case of an uniform electron gas. The local density approximation (LDA) is the simplest way to treat the exchange and correlation. In this method, the exchange and correlation energy density, ε_{xc}^{UEG} , is approached to the value computed in an uniform electron gas at each point in space, $\rho(\mathbf{r}) = \rho$. Hence, the LDA energy can be computed as:

$$E_{xc}^{LDA}[\rho(\mathbf{r})] = \int \rho(\mathbf{r}) \varepsilon_{xc}^{UEG}[\rho] d\mathbf{r}, \quad (2.5.1)$$

In general $\varepsilon_{xc}^{UEG}(\rho)$ can be split into two main terms, the exchange and the correlation such as,

$$\varepsilon_{xc}^{UEG}(\rho) = \varepsilon_x^{UEG}(\rho) + \varepsilon_c^{UEG}(\rho) \quad (2.5.2)$$

where Dirac have proposed the exchange part such as [26]:

$$\epsilon_x^{UEG}(\rho) = -C_x \rho^{1/3}, C_x = \frac{3}{4} \left(\frac{3}{\pi} \right)^{1/3} \quad (2.5.3)$$

and, for the correlation part, there is no exact analytic format existing many different parametrizations.

One natural way to improve the LDA functional is to consider that $\epsilon_{xc}[\rho(\mathbf{r})]$ does not depend only on the electronic density, but it also depends on the gradient of the electronic density in each point of space. This approach is called generalized gradient approximation (GGA) and can be read as:

$$E_{xc}^{GGA}[\rho(\mathbf{r})] = \int \rho(\mathbf{r}) \epsilon_x^{UEG} F_{xc}(\rho, \nabla \rho) d\mathbf{r}. \quad (2.5.4)$$

Where, ϵ_x^{UEG} , is the exchange energy density of the uniform electron gas and $F_{xc}(\rho, \nabla \rho)$ is the GGA enhancement factor depending on a dimensionless density gradient, s , where s is read as

$$s = \frac{|\nabla \rho|}{2k_f \rho}. \quad (2.5.5)$$

In this case, F_{xc} describes the deviations from the uniform electron gas features.

There are many formats for F_{xc} , where, the most usual are the ones proposed by Becke (B88) [27], Perdew and Wang (PW91) [28] and Perdew, Burke and Enzerhof (PBE) [29]. In this thesis, most of the calculations have employed the PBE approximation. Although, GGA functional usually present good predictions for physical and chemical properties, there are specific situations where it displays poor accuracy. Some possibilities are as follows: materials with Van der Waals dispersion interaction [30], strongly correlated materials [31] or properties where the self interaction error can be an issue [32, 33].

2.5.1 Self-Interaction Error

The self-interaction error is the residual interaction of electrons with themselves. In LDA and GGA approaches, the self-interaction coming from the exchange and correlation term do not completely cancel with the Coulomb self-interaction, such as in the Hatree-Fock theory. This effect causes the tendency of spreading out charge instead of localizing it becoming an important issue especially for systems containing strong correlated and highly localized electrons, charged defects and structures in the vicinity of the transition state [34]. Alternatives, employed during the production of this thesis, to partially overcome this problem are to use the DFT+U approach or the hybrid functional scheme.

2.5.2 DFT+U Approach

Compounds presenting localized states such as d or f electrons are not accurately described by GGA or the LDA functional. Part of the unrealistic electronic delocalization displayed by the standard functional is owed to the self-interaction error, as discussed before. One way to properly treat this kind of system is to add a Hubbard like term in the Kohn-Sham Hamiltonian. This approach is denominated DFT+U and it can selectively improve the description of the correlated electrons. Within the DFT+U framework, the energy functional is read as:

$$E_{DFT+U}[\rho(\mathbf{r}), n^\sigma] = E_{DFT}[\rho(\mathbf{r})] + E_U[n^\sigma] + E_{dc}[n^\sigma] \quad (2.5.6)$$

where E_{KS} is the DFT energy functional, E_U concerns to the Hubbard energy correction, E_{dc} comes to remove the contribution of the corrected states already counted in the E_{KS} and n^σ is the density matrix element.

There exist different ways to implement the DFT+U approach onto the ab initio calculations. For instance, Liechtenstein et al. [35] enter with the terms U and J , Hubbard interaction and Hund exchange interaction, respectively, as independent parameters to correct the calculations. In the projects performed during the thesis, all investigations have employed the simplified approach proposed by Dudarev et al. [36]. In this approach, the orbital-dependent interactions are replaced by a spherical average and only a single effective parameter $U_{eff} = U - J$ is used to account for the Hubbard U parameter and the exchange interaction, J . Thus, eq. 2.5.6 is rewritten as:

$$E_{DFT+U}[\rho(\mathbf{r}), n^\sigma] = E_{DFT}[\rho(\mathbf{r})] + \frac{U_{eff}}{2} \sum_{\sigma} Tr(n^\sigma - n^\sigma n^\sigma) \quad (2.5.7)$$

This approach can partially overcome the self-interaction error inherent of the LDA and GGA functional. Therefore, the DFT+U formalism can better describe the localized and strongly correlated states.

2.5.3 Hybrid Functional

The application of hybrid functional emerges as other interesting method going beyond the GGA approach. The main strategy of these set of functional is to partially incorporate the exact exchange in the exchange and correlation term. Hence, part of the self interaction error from the GGA approach is canceled with the inclusion of the exact exchange and the nonphysical electron delocalization displayed in some materials by the GGA functional can be overcome.

The Heyd-Scuseria-Ernzerhof (HSE) [37] functional, the method of choice for in this thesis, takes the form:

$$E_{xc}^{HSE} = \alpha E_x^{SR}(\mu) + (1 - \alpha) E_x^{PBE,SR} + E_x^{PBE,LR}(\mu) + E_c^{PBE} \quad (2.5.8)$$

Where $E_x^{SR}(\mu)$ is the short range exact exchange energy, $E_x^{PBE,SR}$ and $E_x^{PBE,LR}$ are the exchange energies coming from the PBE functional and E_c^{PBE} is the correlation also from the PBE functional. The two parameters, α (mixing parameter) and μ (screening parameter), are concerned the fraction of exact exchange incorporated and the definition of short and long range interactions. In practice, the short and long range interactions are separated by means of an error function,

$$\frac{1}{\mathbf{r}} = \frac{\text{erfc}(\mu\mathbf{r})}{\mathbf{r}} + \frac{\text{erf}(\mu\mathbf{r})}{\mathbf{r}} \quad (2.5.9)$$

and, at long range interaction, the exchange functional is replaced by the PBE exchange. At short range, then, the exact exchange is employed.

2.5.4 Van der Walls Interactions

The formation of organic molecular solids, in many cases, involves with dipole-dipole interactions. These are weak interactions known as Van der Walls (vdW) forces coming from three main sources: permanent dipole forces, induced dipole forces and instantaneously induced dipoles (dispersion interactions). Here, we are going to focus on the dispersion interactions. These are attractive forces with long-range features since it decays with R^{-6} [38], where R is the distances among the concerned group of atoms or molecules. Moreover, organic solids properties are highly connected with the dispersion interactions being, in some cases, the main driven force for the formation of the solid. As discussed before, most of the currently used functional are local or semi-local, then, they are not able to properly describe these long-range forces. It opens the need to incorporate these kinds of interactions within the DFT framework. Indeed, there are many methods to include dispersion interactions with distinct degrees of accuracy and computational cost. One very used scheme is to perform a sum of interatomic pairwise potentials and add it to the DFT energy. Grimme [39–41], Tkatchenko and Scheffler (TS) [42] as well as Becke and Johnson (BJ) [43] are examples of different methods using the concept of adding a potential to account for the dispersion relations. In this thesis, the methods develop by Grimme, known as DFT-D2 and DFT-D3, were employed. These approaches write the corrected total energy, E_{DFT-D} , as $E_{DFT-D} = E_{DFT} + E_{disp}$. For the DFT+D2 the dispersion term is read:

$$E_{disp} = -s_6 \sum_{i < j} \frac{C_6^{ij}}{\mathbf{r}_{ij}^6} \frac{1}{1 + \exp^{-d(R_{ij}/R_r - 1)}} \quad (2.5.10)$$

where s_6 is a global scaling factor, C_6^{ij} is the dispersion coefficient, R_{ij} is the atomic distances, $R_r = R_i + R_j$ is the sum of the van der Walls radii of atom i and j , respectively. Finally, d is an adjustable parameter. Once the parameters

C_6^{ij} , s_6 , $R_r = R_i + R_j$ and d are tabulated, the computation of E_{disp} accounts to a negligible time when compared to the self-consistent field iterations. It is, then, considered a very computationally efficient method. The main drawback of this scheme is the lack of flexibility due to the C_6 coefficient does not consider the local chemical environment. This issue is overcome in the DFT+D3 method. There, the dispersion coefficient is adjustable depending on the coordination number of a specific species.

2.6 Computational Methods

2.6.1 Basis Set

Once the exchange and correlation functional is defined it is possible to compute the Kohn-Sham equations and derive the single particle KS wavefunctions, ψ_i , and eigenvalues, ϵ_i . The construction of the basis set employed to expand ψ_i is, therefore, the next step to solve the KS equations where the KS orbitals are expressed in terms of a set of coefficients $c_{i\mu}$ and a basis set Φ_μ leading to:

$$\psi_i = \sum_{\mu=1}^N c_{i\mu} \Phi_\mu \quad (2.6.1)$$

where N is the number of basis used to describe the orbitals.

The substitution of ψ_i in the KS equations, eq. 2.4.2, by their expansions, reduces the problem to a generalized matrix problem in terms of the KS Hamiltonian and overlap matrix such as:

$$\left[-\frac{\hbar^2}{2m} \nabla^2 + V_{eff}(\mathbf{r}) \right] \sum_{\mu=1}^N c_{i\mu} \Phi_\mu = \epsilon_i \sum_{\mu=1}^N c_{i\mu} \Phi_\mu \quad (2.6.2)$$

where multiplying this equation from the left by the conjugate of the basis functions, Φ^* , and integrating over the volume, it is obtained:

$$\sum_{\mu=1}^N c_{i\mu} \int_r \Phi_\nu^* \hat{h} \Phi_\mu d\mathbf{r} = \epsilon_i \sum_{\mu=1}^N c_{i\mu} \int_r \Phi_\nu^* \Phi_\mu d\mathbf{r} \quad (2.6.3)$$

with

$$\hat{h} = \left[-\frac{\hbar^2}{2m} \nabla^2 + V_{eff}(\mathbf{r}) \right] \quad (2.6.4)$$

The integrals in eq. 2.6.3 are the KS single particle Hamiltonian elements, $H_{\nu\mu}$, and the overlap matrix elements, $S_{\nu\mu}$, respectively. By introducing a matrix for the coefficients, $c_{i\mu}$, and a matrix for the eigenvalues, ϵ_i , the problem is

reduced to a generalized matrix problem in terms of the KS Hamiltonian and overlap matrix S .

$$\mathbf{H}^{\text{KS}}\mathbf{C} = \mathbf{S}\mathbf{C} \quad (2.6.5)$$

and the final solution is obtained by diagonalizing this system of equations.

A natural basis set choice, widely used for molecular systems, is composed of contracted Gaussian functions. In this approach, each basis is written as a linear combination of different Gaussians, $\sum_{s=1}^{NBS} d_{us} \phi_s$, denominated contracted Gaussian Functions (CGF) and involving easy and fast solutions of the Hamiltonian matrix elements. Moreover, this basis can be tuned to have the desired property by varying the presented parameters of the CGF [44]. On the other hand, Plane-Waves (PW) displays important advantages in the treatment of systems with periodic boundary conditions and this is the next topic to be discussed.

2.6.2 Bloch Electrons

In a bulk, the electrons are subjected to an effective potential showing the periodicity of the crystal lattice. Hence, the KS orbitals can be written as a Bloch wave function [31]

$$\psi_k^n(\mathbf{r}) = u_k^n(\mathbf{r})e^{i\mathbf{k}\cdot\mathbf{r}}, \quad (2.6.6)$$

where \mathbf{k} is a vector in the first Brillouin zone and $u_k(\mathbf{r})$ is a function with the same periodicity of the crystal lattice.

In order to solve the KS equations, one can expand $u_k^n(\mathbf{r})$ in a sum of plane waves such that:

$$\psi_k^n(\mathbf{r}) = \frac{1}{\sqrt{\Omega_{cel}}} \sum_j c_j^n(\mathbf{k}) e^{i(\mathbf{k}+\mathbf{K}_j)\cdot\mathbf{r}} \quad (2.6.7)$$

where Ω_{cel} is the volume of the primitive cell, \mathbf{K}_j are reciprocal lattice vectors defined in such a way that $\mathbf{K}_j\cdot\mathbf{R} = 2\pi m$ where m is an integer and \mathbf{R} stands by the real space lattice vectors. Moreover, c_j^n are the coefficients of the expansion and n is the band index.

To solve the KS equations one needs to truncate the basis and consider only values of $\mathbf{k} \leq \mathbf{k}_{\text{max}}$. This means that only the reciprocal lattice vectors inside a \mathbf{k}_{max} radius would be taken into account. Thus, the diagonalization of eq. 2.6.5 with the KS orbitals expanded into a PW basis set produces a set of band indexed eigenvalues $\epsilon_n(\mathbf{k})$ and eigenfunctions, ψ_k^n , as the solution of the band structure problem.

2.6.3 PAW Method

One of the issues to solve Kohn-Sham equations is to deal with the fast oscillations of the one particle wave functions close to the nuclei. The Projected

Augmented Wave (PAW) method [45, 46] originates with the idea of using a linear transformation that maps the total wave function in a smoother auxiliary wave function (named pseudo wave function, PS) computationally more convenient. An augmentation region is defined, Ω , surrounding each ion (core region) of the crystal in non-overlapping fashion. Moreover, an interstitial region is defined as the reminiscent part of the crystal. Outside Ω the true wave function coincides with the pseudo wave function and a set of plane waves are used to expand it. Inside the core region, Ω , a set of partial waves are used to describe the one particle wave functions.

The one particle wave function is denoted as $|\Psi\rangle$ and its transformation (pseudo wave function) as $|\tilde{\Psi}\rangle$. Then the transformation from the pseudo wave function to the true wave function occurs through the T operator such as $|\Psi\rangle = T|\tilde{\Psi}\rangle$. If one knows the format of the transformation between the PS wave function to the total wave function, it becomes possible to compute the expectation value of some physical observable in terms of PS.

To construct the T operator, the first step is to consider that the pseudo wave function and the true wave function both present the same shape far from the core. Furthermore, this transformation leads the total wave function to a smoother wave function (PS) close to the nuclei, avoiding fast oscillations, in each core region. One way to fulfill these requirements is to define T as:

$$T = 1 + \sum_R S_R \quad (2.6.8)$$

where each S_R acts only inside the Ω_R space region close to atom R . The function of the S_R operator is to establish the difference of the true wave function and the pseudo wave function in the core regions.

Now, a new function has been introduced as the partial waves $|\phi_i\rangle$. It is basically the solution of the Schrödinger equation for isolated atoms and S_R is defined in terms of it. Moreover, these set of partial waves will serve as the basis set to expand the true valence wave function close to the nuclei (inside Ω) with unknown coefficients for now.

$$|\Psi\rangle = \sum_i c_i |\phi_i\rangle \rightarrow \text{Inside } \Omega_R \quad (2.6.9)$$

One requirement for the set of partial waves $|\phi_i\rangle$ is that it should include only states that are orthogonal to the core wave functions. Now, we define a set of functions $|\tilde{\phi}_i\rangle$ where the application of T leads to the partial waves $|\phi_i\rangle$

$$|\phi_i\rangle = T |\tilde{\phi}_i\rangle \quad (2.6.10)$$

$$|\phi_i\rangle = (1 + S_R) |\tilde{\phi}_i\rangle \quad (2.6.11)$$

$$S_R |\tilde{\phi}_i\rangle = |\phi_i\rangle - |\tilde{\phi}_i\rangle, \quad (2.6.12)$$

from eq. 2.6.11, the contribution of the local operator S_R is defined in terms of $|\phi_i\rangle$ and $|\tilde{\phi}_i\rangle$. Since T acts only inside Ω , it is required that $|\phi_i\rangle$ and $|\tilde{\phi}_i\rangle$ have to be equal outside Ω .

Now, a projector operator, $|\tilde{p}_i\rangle$, is defined following the conditions: $\langle \tilde{p}_i | \tilde{\phi}_j \rangle = \delta_{ij}$ to $i, j \in R$ and $\sum_i |\tilde{\phi}_i\rangle \langle \tilde{p}_i| = 1$, inside Ω . The projector function has to be orthogonal to the pseudo wave function (PS) inside Ω and it leads to $c_i = \langle \tilde{p}_i | \tilde{\Psi} \rangle$, then, we can write:

$$|\tilde{\Psi}\rangle = \sum_i c_i |\tilde{\phi}_i\rangle \quad (2.6.13)$$

$$|\tilde{\Psi}\rangle = \sum_i |\tilde{\phi}_i\rangle \langle \tilde{p}_i | \tilde{\Psi} \rangle. \quad (2.6.14)$$

This equation states that the PS wavefunction can be expanded in terms of the pseudo partial waves inside the core region. Then, applying S_R in $|\tilde{\Psi}\rangle$

$$S_R |\tilde{\Psi}\rangle = \sum_{i \in R} S_R |\tilde{\phi}_i\rangle \langle \tilde{p}_i | \tilde{\Psi} \rangle = \sum_{i \in R} (|\phi_i\rangle - |\tilde{\phi}_i\rangle) \langle \tilde{p}_i | \tilde{\Psi} \rangle \quad (2.6.15)$$

then

$$|\Psi\rangle = T |\tilde{\Psi}\rangle \quad (2.6.16)$$

$$|\Psi\rangle = |\tilde{\Psi}\rangle + \sum_i (|\phi_i\rangle - |\tilde{\phi}_i\rangle) \langle \tilde{p}_i | \tilde{\Psi} \rangle \quad (2.6.17)$$

where

$$T = 1 + \sum_i (|\phi_i\rangle - |\tilde{\phi}_i\rangle) \langle \tilde{p}_i | \quad (2.6.18)$$

The first term on the right side of eq. 2.6.17 represents the pseudo wave function. Outside Ω it would be equal to the EA, $|\Psi\rangle = |\tilde{\Psi}\rangle$. The second term is related to the partial wave function that is chosen as the solution of the Schrödinger equations for isolated atoms and $|\tilde{p}_i\rangle$ are the projector functions. The third term has the goal of canceling the contributions of the pseudo wave function inside Ω . It also acts to cancel the contribution of the partial wave function in the interstitial region. These three contributions and the way they match in the limit of Ω are the basis of PAW method.

2.7 Force Theorem

The process to reach the structure with minimum energy is usually based on the following idea: Considering F_k as the force felt by a nucleus at position k in a crystal lattice, then F_k can be expressed like

$$F_k = -\nabla_{R_k} E, \quad (2.7.1)$$

where

$$E = \frac{\langle \psi | H | \psi \rangle}{\langle \psi | \psi \rangle} \quad (2.7.2)$$

and, assuming that $\langle \psi | \psi \rangle = 1$, we can substitute eq. 2.7.2 into eq. 2.7.1 finding:

$$F_k = - \left\langle \psi \left| \frac{\partial H}{\partial R_k} \right| \psi \right\rangle - \left\langle \frac{\partial \psi}{\partial R_k} | H | \psi \right\rangle - \left\langle \psi | H | \frac{\partial \psi}{\partial R_k} \right\rangle. \quad (2.7.3)$$

If the following conditions are true: $H|\psi\rangle = E|\psi\rangle$ and $\langle \psi | \psi \rangle = 1$, then the third and fourth terms of eq. 2.7.3 goes to zero and the force can be expressed as:

$$F_k = - \frac{\partial \langle \psi | H | \psi \rangle}{\partial R_k} = - \left\langle \psi \left| \frac{\partial H}{\partial R_k} \right| \psi \right\rangle. \quad (2.7.4)$$

This equation stands for the Hellmann-Feynman theorem establishing that the derivative of the energy with respect to any parameter is equal the expectation value of the Hamiltonian's derivative. In real electronic structure calculation, the Hellmann-Feynman theorem is called to derive the ground state structure of a required physical system. This process is done by computing the forces felt by a set of nuclei and, then, moving this set of atoms in such a way that the total energy of the system becomes lower and the forces go to zero.

3. Ionic Diffusion

3.1 Molecular Dynamics

The main concept behind molecular dynamics simulations comes from Newton's second law. The atomic nuclei in a many body system are considered as classical particles, hence, the atomic motion is governed by the relation

$$\mathbf{F}_i = m_i \mathbf{a}_i \quad (3.1.1)$$

where \mathbf{F}_i is the force on the atom i , m_i is its mass and \mathbf{a}_i is the acceleration felt by the atom i . This is a second order differential equation that can be integrated by applying, for instance, the Verlet algorithm. This method uses a Taylor expansion of \mathbf{r} in two time steps, $\mathbf{r}(t + \Delta t)$ and $\mathbf{r}(t - \Delta t)$ and subtracts them. This procedure results in the relation, $\mathbf{r}(t + \Delta t) \simeq 2\mathbf{r}(t) - \mathbf{r}(t - \Delta t) + \frac{\mathbf{F}_i(t)}{m_i} \Delta t^2$, that correlates the atomic positions at time $(t + \Delta t)$ with previous timesteps (t) and $(t - \Delta t)$. The main advantage of this algorithm is that after the subtraction of the Taylor expansion the odd power terms disappear inducing an error of the order of Δt^4 .

In the recent years, the advances in electronic structure methods have made possible the evaluation of forces on the atomic nuclei by means of first principle calculations. This method is generally known as *ab initio* molecular dynamics (AIMD) and it allows the performance of simulations without any empirical parameter. The AIMD has two main implementations: Car-Parrinello and Born-Oppenheimer. They differ on the basis that forces acting on the nuclei are computed where the Car-Parrinello algorithm solves the electronic and the nuclei problem at the same time with the help of a fictitious Lagrangian while the Born-Oppenheimer approach separates the electronic and nuclei parts with the nuclear dynamics dictated by the electronic potential energy surface. In this thesis, the Born-Oppenheimer method is applied to compute the required kinetic properties.

The investigation of ionic diffusion into a host crystal structure, for instance, can be studied by applying the AIMD framework. The initial step for such a simulation is to equilibrate the system to a specific thermodynamic state or ensemble. Once the system reaches the equilibrium, one can accumulate sufficient information, for example the particle trajectory, to finally compute the required property by an averaging process. A canonical ensemble is used where particles number N , volume V and temperature T are maintained constant. The controlling of the target temperature is obtained by applying

different methods. Among them, the velocity rescaling is the most straightforward procedure. It uses the equipartition theorem to correlate temperature with the nuclei velocities and to maintain the target temperature. A simple extension of the velocity scaling scheme is to use a weak coupling with the thermal bath, as proposed by Berendsen et al. [47]. In this case, the velocities are not rescaled each time step of the simulation. Instead, a time interval, τ , is added to allow heat exchange with the bath in such a way that τ is bigger than Δt (time step). There is no proof that this method reproduces the canonical ensemble. On the other hand, Berendsen showed that weak coupling leads to the correct canonical averages. Another common strategy to control the target temperature was proposed by Nosé and Hoover [48, 49]. In this method, a fictitious degree of freedom s is added to the energy function that represents the heat bath. Moreover, an extended Lagrangian is written by considering the particles as well as the heat reservoir. Then, it can be shown that the molecular dynamics of the extended system produce a canonical ensemble.

In this thesis, most of the AIMD simulations were performed with the aim of studying atomic diffusion mechanisms. One important quantity that can be extracted from the individual atomic positions as a function of time is the mean squared displacement (MSD). This quantity can be read as:

$$MSD = \langle \sum_i^N [\mathbf{r}_i(t) - \mathbf{r}_i(0)]^2 \rangle \quad (3.1.2)$$

where N stands for the number of particles in the unit cell. $\mathbf{r}_i(t)$ and $\mathbf{r}_i(0)$ are the respective positions at time t and 0 . This quantity is related to the Einstein relation by:

$$MSD = 6Dt + C \quad (3.1.3)$$

where D is the diffusion coefficient. It means that with the MSD in the linear regime, it is possible to derive the diffusion coefficient by fitting eq. 3.1.3 to the data and extracting the slope of it.

3.2 Transition State Theory

Some of the mechanisms of diffusion investigated in this thesis deal with activated process. To clarify this point let us analyze Figure 3.1. There, one can see that an atom X is in the equilibrium position A . To ensure the diffusion of this atom from the position A to the new equilibrium position B , it must accumulate an energy bigger than the displayed activation energy E_a . In the cases where the activation energy is much bigger than the thermal energy, the application of AIMD becomes unrealistic due to the large time scale needed to observe this process in the simulation. Hence, we need to turn to a different method to understand the migration mechanisms.

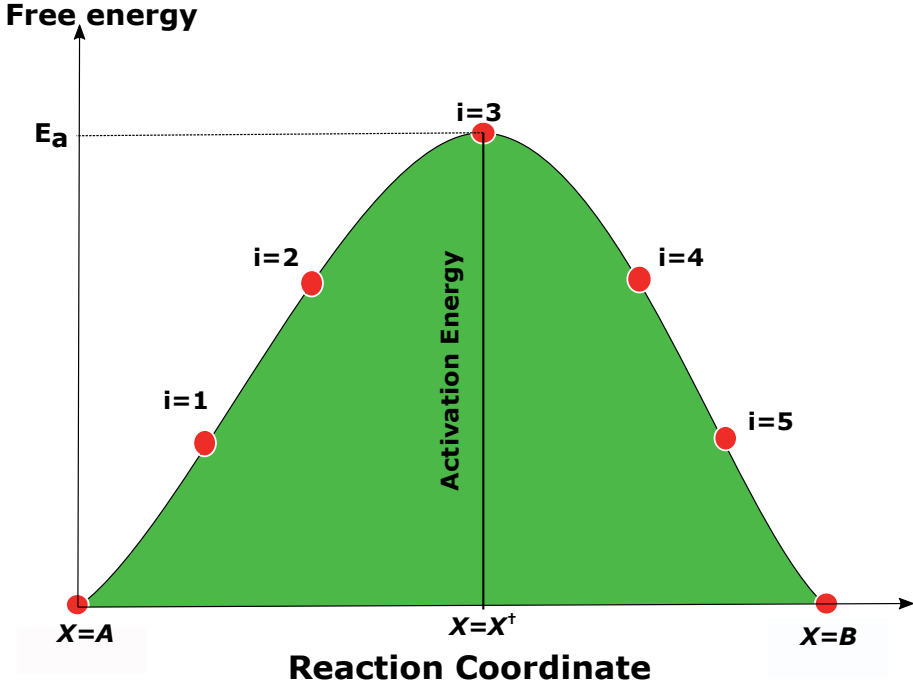


Figure 3.1. The activation energy for an atom X at equilibrium position A jump to the equilibrium position B. The red points indicate the images created in the Nudged Elastic Band method.

The transition state theory (TST) provides us with the framework to investigate the migration mechanisms of an activated process like the case in Figure 3.1. To get some insights of this theory, an unidirectional problem is initially considered. For this case, the reaction rate, $k_{A \rightarrow B}$, of a process as described in Figure 3.1 is obtained as:

$$k_{A \rightarrow B} = \frac{1}{2} \times \text{average velocities of the species} \\ \times \text{probability of finding the particle in the transition state} \quad (3.2.1)$$

The probability of finding the particle in the transition state, $x = x^\ddagger$, is read as:

$$P(x^\ddagger) = \frac{\int_{\ddagger} dx e^{\beta E(x^\ddagger)}}{\int_A dx e^{\beta E(x)}}, \quad (3.2.2)$$

where \ddagger denotes the transition state, the denominator of eq. 3.2.2 is the partition function of the reactant (initial state of the system) and the numerator is the partition function of the transition state.

The calculation of the velocities is performed by doing an averaging of the particle moment by considering that they show the same value at any point:

$$\langle p \rangle = \frac{\int_p |p| e^{-p^2/2mkT} dp}{\int_p e^{-p^2/2mkT} dp} = \frac{2mkT}{\sqrt{2\pi mkT}} = \sqrt{\frac{2mkT}{\pi}} \quad (3.2.3)$$

$$\langle v \rangle = \sqrt{\frac{2kT}{\pi m}} \quad (3.2.4)$$

where v is the average velocities and m is the mass of the atom.

Now, we are able to come back to the eq. 3.2.1 and substitute the referent quantities and to compute the rate of the concerned reaction. By doing so, the following expression is derived:

$$k_{A \rightarrow B} = \frac{1}{2} \sqrt{\frac{2}{\beta \pi m}} \frac{\int_{\ddagger} dx e^{\beta E(x^{\ddagger})}}{\int_A dx e^{\beta E(x)}} \quad (3.2.5)$$

where $E(x^{\ddagger})$ is the energy of the system in the transition state and $\beta = \frac{1}{k_B T}$.

The next step is to use the harmonic approximation. This approach consider small variations of particles position in respect to the equilibrium state. Therefore, the energy, $E(x)$ in eq. 3.2.5 can be Taylor expanded as $E(x) \cong E(A) + \frac{k}{2}(x - x_A)^2$. Here, $E(A)$ is the particle energy at the equilibrium position and $\frac{k}{2}(x - x_A)^2$ is the harmonic potential. The application of the harmonic approach to the transition state comes with a consideration. Indeed, the width of the transition state surface in the x direction is so small that the potential is assumed to be a constant at this point. Then, the application of the harmonic approximation allowed as to compute the integrals of eq. 3.2.5 as:

$$\int_A dx e^{\beta E(x)} \cong e^{\beta E(A)} \int_{-\infty}^{+\infty} dx e^{\beta k(x - x_A)^2/2} = \sqrt{\frac{2\pi}{\beta k}} e^{\beta E(A)} \quad (3.2.6)$$

$$\int_{\ddagger} dx e^{\beta E(x)} \cong e^{\beta E(x^{\ddagger})} \quad (3.2.7)$$

and substituting their results in eq. 3.2.2 and together with the relation $v = \frac{1}{2\pi} \sqrt{\frac{k}{m}}$, the reaction rate final format is:

$$k_{A \rightarrow B} = v \exp \left(\frac{E(x^{\ddagger}) - E(A)}{k_B T} \right) \quad (3.2.8)$$

All the theoretical analysis performed above stands for an uni-dimensional diffusion case. However, the same framework can be used to derive the reaction rate of a general case. This complex problem is simplified by describing the system in terms of the coordinates corresponding to the normal modes of vibration and the final result of the general case goes to:

$$k_{A \rightarrow B} = \frac{v_1 \times v_2 \times \dots \times v_N}{v_1^\ddagger \times \dots \times v_{N-1}^\ddagger} \exp\left(\frac{\Delta E}{k_B T}\right) \quad (3.2.9)$$

where ΔE is the activation energy, v is the vibrational frequencies of the reactant and v^\ddagger is the real vibrational frequencies of the saddle point. The imaginary frequency corresponding to the unstable vibrational mode at the transition state is removed from the denominator product.

It is worth to mention that the obtained results for the reaction rate agree well with the empirical observed Arrhenius expression for the reaction rate, $k = v e^{\frac{-\Delta E}{k_B T}}$ where A is the attempt frequency.

3.3 Finding the Saddle Point

One of the most applied methods to find the transition state of a reaction, with the framework of the density functional theory, is the Nudged Elastic Band (NEB) method. H. Jónsson *et. al.* [50] developed the NEB as an enhancement of the chain of states method where the main goal is to find the minimum energy pathway (MEP) of a reaction. This method has been widely employed in many investigations in order to bring out insights related to diffusion mechanisms. The NEB is a robust technique for seeking the reaction pathway and the saddle point along the MEP between two previously known end points.

The best way to understand how the NEB framework works is showing its strategy to move a set of images (reaction coordinates) into the MEP. Initially, it linearly interpolates a number of images (replicas of the system that we will call i as represented in Figure 3.1) between two equilibrium points, A and B, in the energy landscape. All intermediate replicas, i , must exhibit a resultant force on each atom since they are not in an equilibrium position ($\mathbf{F}_{total} = -\nabla E \neq 0$). Then, these forces are decomposed in two main directions: one perpendicular to a unitary vector, $\hat{\tau}_i$, pointing along a direction defined by the two adjacent images and another one in the same direction of $\hat{\tau}_i$. The chain of images will satisfy the MEP condition if the force acting perpendicularly to the chain direction, $\hat{\tau}_i$, is zero. This condition suggests to use a force projection scheme of the images in which the perpendicular component of \mathbf{F}_{total} decreases. Moreover, a harmonic potential is included in the direction of $\hat{\tau}_i$ between the images. The final direction where the images have to move is defined by the force:

$$\mathbf{F}_{i,NEB} = \mathbf{F}_i^\perp + \mathbf{F}_{i,mola} = \mathbf{F}_i^\perp + k(\mathbf{r}_{i+1} - \mathbf{r}_i) \quad (3.3.1)$$

where \mathbf{F}_i^\perp is the force perpendicular to the chain direction, $\hat{\tau}_i$, and the last term of eq. 3.3.1 is the spring force acting in the direction of $\hat{\tau}_i$.

3.4 Case 01: Ionic Migration in $\text{Li}_2\text{FeSiO}_4$

LiFeSiO_4 was firstly proposed as a cathode of Li rechargeable battery by Nytén et al. [51]. This compound represents a low cost alternative with good device performance in comparison to the currently used materials LiFePO_4 and LiCoO_2 . Nytén has proposed an orthorhombic lattice with $\text{Pmn}2_1$ space group. At the same time, another polymorph of LiFeSiO_4 was proposed by Nishimura et al. [52] with a monoclinic structure and $\text{P}2_1$ space group. Both the structures are formed by composite layers of SiFeO_4 where the FeO_4 and SiO_4 form shared corner tetrahedra. Lithium ions are located between the layers also forming LiO_4 tetrahedral. The main difference between the polymorphs with orthorhombic and monoclinic structures is the alignment of the FeO_4 and SiO_4 units. For the orthorhombic case, they point in the same direction while the monoclinic structure has the tetrahedra aligned in alternate directions. The structures are represented in Figure 3.2.

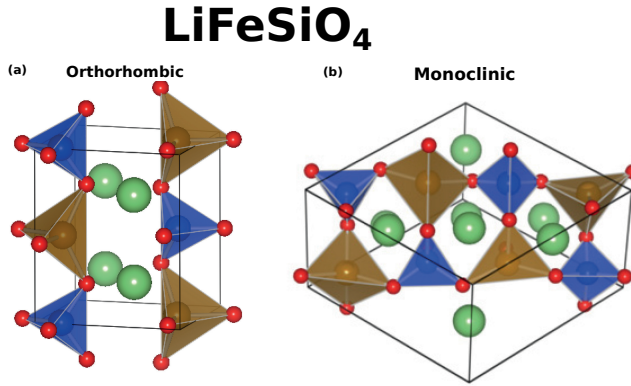


Figure 3.2. Crystal structures of $\text{Li}_2\text{FeSiO}_4$ in the orthorhombic (a) and the monoclinic (b) symmetries. Here, red spheres represent oxygen, blue spheres (inside semi-transparent blue tetrahedra) represent silicon, brown spheres (inside semi-transparent brown tetrahedra) represent iron, while green spheres represent lithium ions.

The primary goal of this section is to use the formalism of the nudged elastic band method to investigate the ionic diffusion mechanism into the crystal lattice of $\text{Li}_2\text{FeSiO}_4$. Two main questions were investigated. The first one concerns the effects of the Hubbard term in the computation of activation energies. These compounds contain Fe ions with high localized 4d states. Then, the introduction of the U term in the Kohn-Sham Hamiltonian is an important aspect to proper modeling the polyanions. The second question is related

Table 3.1. Results for hopping distance and activation barrier calculations (ΔE) in monoclinic $\text{Li}_2\text{FeSiO}_4$ and LiFeSiO_4 with both GGA and GGA+U formalism.

$\text{Li}_2\text{FeSiO}_4$	Functional	Distance (\AA)	ΔE (eV)
Pathway A	GGA	3.5	1.06
	GGA+U	3.7	0.84
Pathway B	GGA	3.9	1.21
	GGA+U	3.9	0.95
Pathway C	GGA	4.7	1.80
	GGA+U	4.8	1.79
LiFeSiO_4	Functional	Distance (\AA)	ΔE (eV)
Pathway A	GGA	3.00	0.40
	GGA+U	2.76	0.56
Pathway B	GGA	4.00	0.42
	GGA+U	3.72	0.36
Pathway C	GGA	4.70	1.62
	GGA+U	5.05	1.76

to the difference in the diffusion mechanisms when the monoclinic or the orthorhombic structures are considered.

3.4.1 The Effects of the U Term in the Activation Energy

The first step of this part was to set up the U parameter that best model the monoclinic $\text{Li}_2\text{FeSiO}_4$. We have used $U = 5$ eV, which was shown by previous investigations [53, 54] to be a suitable value to reproduce features such as the open circuit voltage. The following task was to determine the most likely pathways for the Li^+ diffusion in the crystal structure. Three main possibilities were considered, as described in Figure 3.3. Pathway A is characterized by a zig-zag trajectory while pathway B comes with a linear ionic migration. For both of these cases, Li^+ ions hop between equilibrium position in the layers formed by Si-Fe-O atoms. The pathway C represents the possibility of ions to cross the layers.

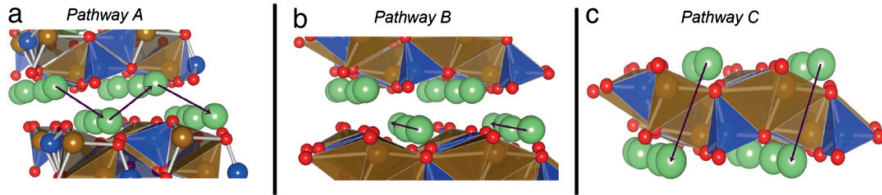


Figure 3.3. Three possible pathways for Li ion migration in monoclinic $\text{Li}_2\text{FeSiO}_4$.

The NEB calculations on the lithiated compound, $\text{Li}_2\text{FeSiO}_4$, in the monoclinic structure displayed a minimum activation energy for pathway A, as shown in Tab. 3.1. It produces a zigzag diffusion process between the Fe-Si-O layers (pathway A). However, the activation barrier calculated for pathway B is quite close to that for pathway A, thus both paths contribute to the Li ion migration. The inclusion of the Hubbard term did not change the most likely path, however, it has considerably diminished the absolute value of the activation energy of pathway A and B, as shown in Table 3.1. The GGA + U scheme leads to a change of the electronic structure, particularly localizing the electrons. It suggests that the resultant Coulombic interaction felt by the Li^+ ion, at the saddle point, for the GGA + U method is quite different as compared to the GGA case producing different activation energies.

Calculations for the delithiated system reveal two different situations: when the Hubbard term is not added, the Li migration can hop through both paths A and B; however, within the GGA + U scheme one of the path becomes more probable. The reason for this effect is the inclusion of the Hubbard term that leads to an activation energy difference between pathway A and B, making pathway B the most probable one. These results emphasize the importance of taking into consideration the U term in the Kohn-Sham Hamiltonian when using the NEB method to compute activation energy of ionic hopping in materials where localized $4d$ states are present.

3.4.2 Monoclinic vs. Orthorhombic Structures

The results of the underlying ionic diffusion mechanism in the orthorhombic crystal structure show some distinct features when compared to the monoclinic polymorph, as observed in Figure 3.4. In the orthorhombic structure, the most likely path is pathway B with an activation barrier of the order of 0.88 eV while pathway A presents a barrier amounting to 0.98 eV. It is important to highlight that, due to the alternative alignment of the FeO_4 tetrahedral, Li^+ ions migrate in a sort of zig-zag diffusion in the monoclinic system while the orthorhombic structure, with aligned FeO_4 tetrahedral, have the ions following a straight line diffusion.

3.5 Case 02: Na Diffusion in $\text{Na}_{2.5}\text{Mn}_{1.75}(\text{SO}_4)_3$

Recently, $\text{Na}_{2+2x}\text{Mn}_{2-x}(\text{SO}_4)_3$ has been proposed as a new candidate cathode of sodium batteries. This compound has an alluaudite structure belonging to the C2/c space group, as depicted in Figure 3.5. The $\text{Na}_{2+2x}\text{Mn}_{2-x}(\text{SO}_4)_3$ crystal structure shows octahedral Mn sites, MnO_6 , with shared oxygen atoms forming bi-octahedral units, Mn_2O_{10} . These units are also repeatedly connected with tetrahedral SO_4 units forming a diffusion path along the $[0\ 0\ 1]$ direction. It has been already [55] reported that sodium atoms are distributed

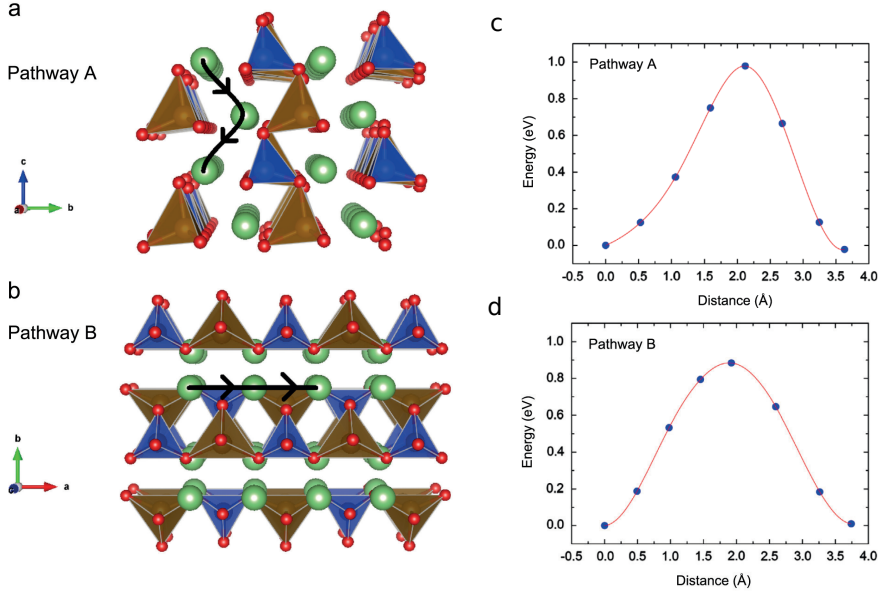


Figure 3.4. (a) and (b) Two most likely diffusion paths in orthorhombic $\text{Li}_2\text{FeSiO}_4$. (c) and (d) the activation energy for the respective pathways.

among three main fractional coordinated sites, Na1, Na2 and Na3, where each of them, present 1, 0.64 and 0.80 partial occupancies, respectively. Moreover, the creation of Mn vacancies give rise to a new fractional position, populated by the sodium excess, named now on NaMn.

Two main questions are investigated in this work. The first concerns to the formation energy of anti-site defects. It is already known that, for materials displaying one dimensional ionic diffusion such as LiFePO_4 , these defects can block the ionic migration. This hinders the performance of the device [56]. The second topic concerns the effects of Mn vacancies in the ionic diffusion procedure.

The formation energy of anti-site defects, where Na^+ exchanges position with one Mn^{2+} was calculated for $\text{Na}_{2.5}\text{Mn}_{1.75}(\text{SO}_4)_3$. Three distinct possibilities have been considered for the formation of these defects where the Mn^{2+} ions undergo an exchange of position with sodium ions occupying Na1, Na2 and Na3 positions. The lower anti-site formation energy is 1.83 eV characterizing it as an unfavorable defect due to the high formation energy value. This result is in contrast with very well established materials such as LiMPO_4 (M= Fe, Mn and Co) [56, 57]. In this poly-anion, the exchange of transition metals with Li^+ is an issue blocking the migration of Li^+ ions. Therefore, it

is not expected that the ionic migration is influenced by this sort of defects in the alluaudite compound.

Four main possible ionic diffusion pathways were investigated employing the formalism of the cNEB method in conjunction with the DFT to have some insights of the main mechanisms of diffusion in the $\text{Na}_{2.5}\text{Mn}_{1.75}(\text{SO}_4)_3$ crystal structure. In the first case, Na hops through the $[0\ 0\ 1]$ direction with the V_{Na} vacancy moving from Na2 to Na2 positions. The second path is also in the $[0\ 0\ 1]$ direction, however, the ions move through the Na3 positions. The third pathway represents the hopping from Na3 to Na1 and then to Na2 coordinates. The fourth pathway accounts for the migration between Na2 to NaMn and then going to Na3 position. Figure 3.5 represents these possibilities. It is observed that the hopping between Na3 positions (path 01) along the $[0\ 0\ 1]$ direction is the most suitable pathway with 0.31 eV activation energy. However, the Mn deficiency blocks the ionic diffusion creating a barrier as high as 0.76 eV for the one dimensional migration, as shown in Figure 3.5. With this scenario, the ionic diffusion turns to an alternative mechanism hopping from $\text{Na3} \rightarrow \text{Na1} \rightarrow \text{Na2}$ (path 03) with an activation energy of 0.58 eV. This pathway points to the $[0\ 1\ 0]$ direction working as a link between the diffusion of $\text{Na2} \rightarrow \text{Na2}$ and $\text{Na3} \rightarrow \text{Na3}$ hops. These results confirm that good kinetic properties are expected when $\text{Na}_{2.5}\text{Mn}_{1.75}(\text{SO}_4)_3$ is employed as a cathode material even though the Mn vacancies partially block the Na diffusion.

3.6 Case 03: Ionic Diffusion in $\text{Na}_x\text{Fe}(\text{SO}_4)_2$

$\text{Na}_2\text{Fe}(\text{SO}_4)_2$ shows a monoclinic crystal structure with a space group C2/m, as depicted in Figure 3.6 (a). In this compound, Na^+ and Fe^{2+} cations are arranged in different ab planes along c direction. The six-oxygen coordinated Fe-polyhedra, FeO_6 , are corner shared by SO_4 tetrahedra. Therefore, each FeO_6 octahedra is connected with six SO_4 units. The shape of the $\text{NaFe}(\text{SO}_4)_2$ crystal structure suggests an ionic diffusion process occurring between the layers of the material. In order to have insights of the Na^+ migration mechanisms, AIMD simulations were performed in conjunction with the NEB method. For the AIMD, temperatures from 900 K up to 1500 K were considered in the canonical ensemble (fixed particle number, volume, and temperature, NVT). The choice of these temperatures aims to accelerate the dynamic of the ions migration. A time step of 2 fs was employed with a total simulation time of 50 ps. The Na^+ ions trajectory coming from the AIMD simulation reveals a hopping mechanism between the two nonequivalent considered Na fractional coordinates. In most of the cases, the Na^+ ions jump from the Na1 position to the Na2 and from Na2 back to Na1, as shown in Figure 3.6 (b). The simulations confirm the expected ionic diffusion through the layers of the material.

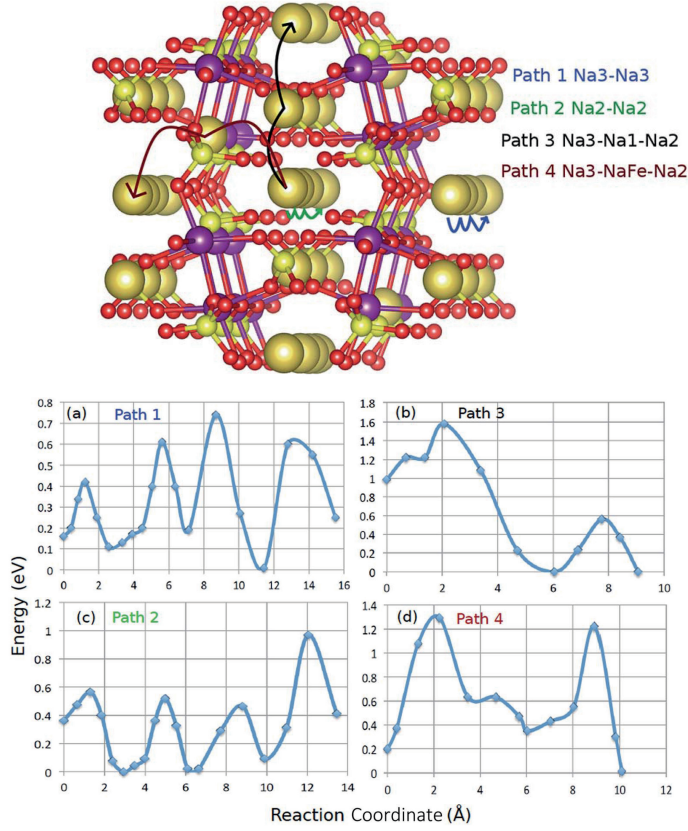


Figure 3.5. Four possible pathways for Na ion migration in $\text{Na}_{2.5}\text{Mn}_{1.75}(\text{SO}_4)_3$.

From the slope of the Arrhenius plot and considering the Arrhenius relation,

$$D = \nu e^{-\frac{\Delta E}{k_B T}}, \quad (3.6.1)$$

where D is the diffusion coefficient, ΔE is the activation energy and ν is the attempt frequency, it is possible to estimate the activation energy of the ionic jumps in $\text{Na}_2\text{Fe}(\text{SO}_4)_2$. Figure 3.6.1 displays the Arrhenius plot at temperatures of 900 K, 1000 K, 1100 K, 1200 K, 1300 K and 1500 K. The derived activation energy amounts to 0.58 eV. The results of the NEB calculations are in good agreement with the obtained results from AIMD. The average activation energy coming from the NEB is 0.64 eV while the AIMD shows 0.58 eV of activation energy with a negligible difference of only 0.06 eV.

The AIMD simulations for the half-sodiated compound, $\text{NaFe}(\text{SO}_4)_2$, did not present any atomic diffusion. This is due to the high activation energy experimented by the Na hop in this material. The solution is, then, to focus

on the results coming from the NEB method. Two main possibilities were investigated: the monovacancy diffusion and the divacancy diffusion. Both the mechanisms present high activation energies with values of 1.15 eV to 1.13 eV. These results indicate a very poor reaction rate with low diffusion coefficient.

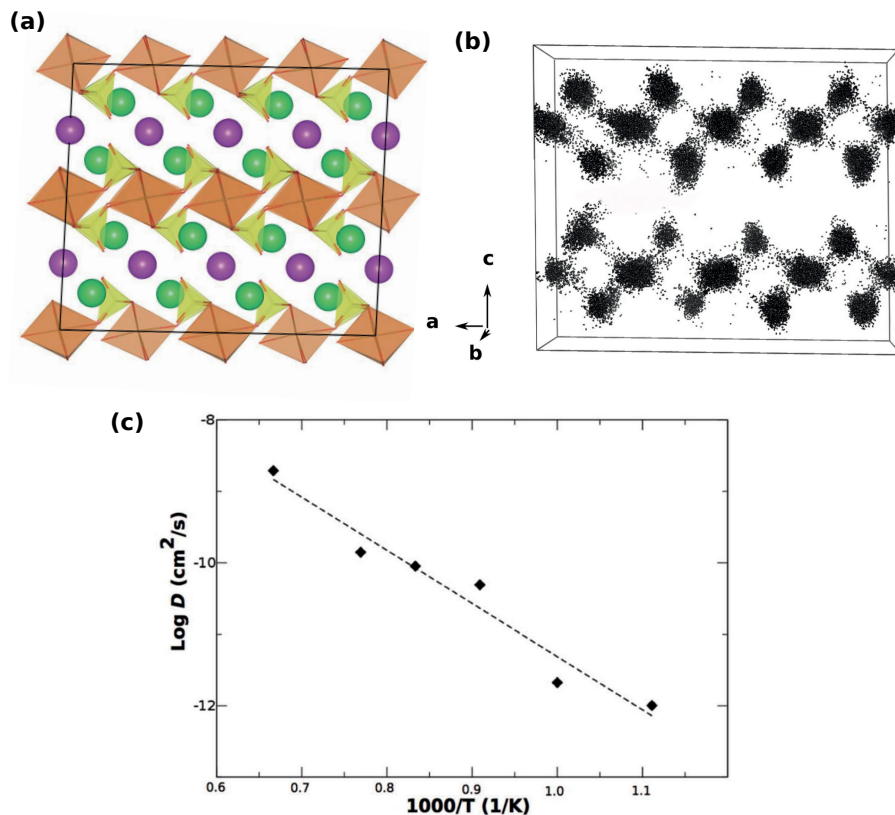


Figure 3.6. (a) Crystal structure of $\text{Na}_2\text{Fe}(\text{SO}_4)_3$. (b) Na ions trajectories over the simulated time scale at 1500 K. (c) Arrhenius plot for $\text{Na}_2\text{Fe}(\text{SO}_4)_2$.

3.7 Case 04: Polaron Migration Mechanism in Na_2O_2

The main goal of this investigation is to unveil the mechanisms of charge transport in sodium peroxide Na_2O_2 . This material is a byproduct of the Na-air battery device and the understanding of the charge diffusion through it is important to enhance the performance of the battery. Figure 3.7 represents the operation of a Na-air battery. There, it is possible to see a sodium peroxide

layer formed on top of the carbon based cathode. The kinetics of the reaction to form Na_2O_2 is constrained by the charge transport from the carbon based cathode to the top of the peroxide compound. Three main models can be thought for the charge diffusion in this system: the first accounts for the migration of small charged defects. The second takes into account the presence of dopants causing the conduction and, finally, the migration through interfaces of different grains of the byproduct. The case of the charge migration through small defects hop is the one investigated in this thesis. More specifically, three small lattice defects are considered as charge carriers: electron polarons, p^- , hole polarons, p^+ , and charged sodium vacancies, V^- .

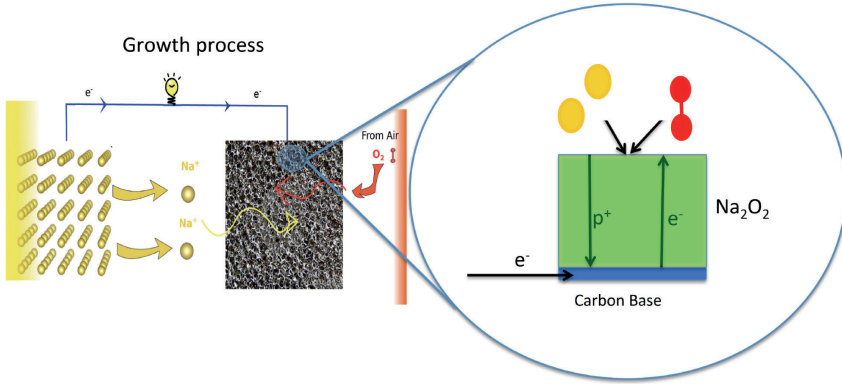


Figure 3.7. Schematic picture of a sodium air battery. The zoom in the cathode illustrate the battery reaction at the atomic level. A carbon based material is used as the cathode. Sodium ions coming from the electrolyte, electrons coming from the carbon based system and oxygen from the air will react to finally form the product of the battery reaction on top of the carbon based electrode.

The first step in this study was to compute the formation energy (E_f) of such defects. In this scenario E_f is evaluated as:

$$E_f(X^q) = E_0(X^q) - E_0(\text{bulk}) - \sum_i n_i \mu_i + e\epsilon_F + \Delta E \quad (3.7.1)$$

where n_i is corresponding to the number of atoms of species i removed or added to the supercell. μ_i is the chemical potential of species i in the considered reservoir. The Fermi level (ϵ_F) in eq. 3.7.1 is fixed with the constraining of the electroneutrality of the compound. The final term of eq. 3.7.1 is the finite size correction. This term is responsible for accelerating the formation

Table 3.2. *Equilibrium defect formation energies (E_f) in eV.*

Defect	E_f
p^+	0.81
p^-	1.82
V_{Na}^-	0.81

energy convergence with respect to the supercell size. Here, the Markov-Payne monopole correction is applied, ΔE , [58] assuming the form:

$$\Delta E = \frac{q^2 \alpha_M}{2\epsilon L} \quad (3.7.2)$$

where α_M is the Madelung constant, L is the volume of the supercell, ϵ is the dielectric constant and q is the net charge of the system. The results of the formation energies are summarized in Table 3.2. It is important to point out that the following results were computed by applying the hybrid functional formalism (HSE06) with 35 % of exact exchange. The application of this level of theory is crucial to properly describe the formation energy of the polaron defects since it can partially overcome the self-interaction error with the incorporation of a fraction of the exact exchange.

Hole polarons, p^+ , appear as one of the intrinsic defects with smaller formation energy. This defect is a result of the electron removal from the Na_2O_2 crystal structure forming a hole in the valence band. The hole tends to be localized in one of the peroxide molecules forming a superoxide ion, O_2^{-1} . This empty state populates a π^* antibonding orbital of an O_2 unit. The electron polarons, p^- have similar features when compared with the hole polaron. It displays a stable state when localized in one of the peroxides forming O_2^{-3} . The formation energy of the electron polaron, on the other hand, is quite high in comparison to the other considered defects. The charged sodium vacancy defect presents a small formation energy, similar to the calculated value for the hole polaron. These results indicate that the charge neutrality principle is reached when the concentration of this defect, charged sodium vacancy, becomes equal to the concentration of the hole polarons, since the higher formation energy of the electron polaron would produce a rather small concentration of this sort of charge carrier.

Figure 3.8 (a) and (b) depicts the investigated migration pathways considered during the investigation of the charge diffusion. For the case of charged vacancies acting as the charge carrier, three main paths come as the most likely. The resulting energy barriers for the V_{Na}^- migration reach to 0.51 eV and 0.50 eV, for paths 01 and 02, respectively. The path 03 has displayed a high activation energy, then, inducing very small probability of diffusion in this direction. Figure 3.8 (b) depicts the migration paths accounted for the diffusion of electron and hole polarons with two possibilities: interlayer and intralayer paths. Figure 3.8 (c) and (d) presents the activation energies of the hole and the elec-

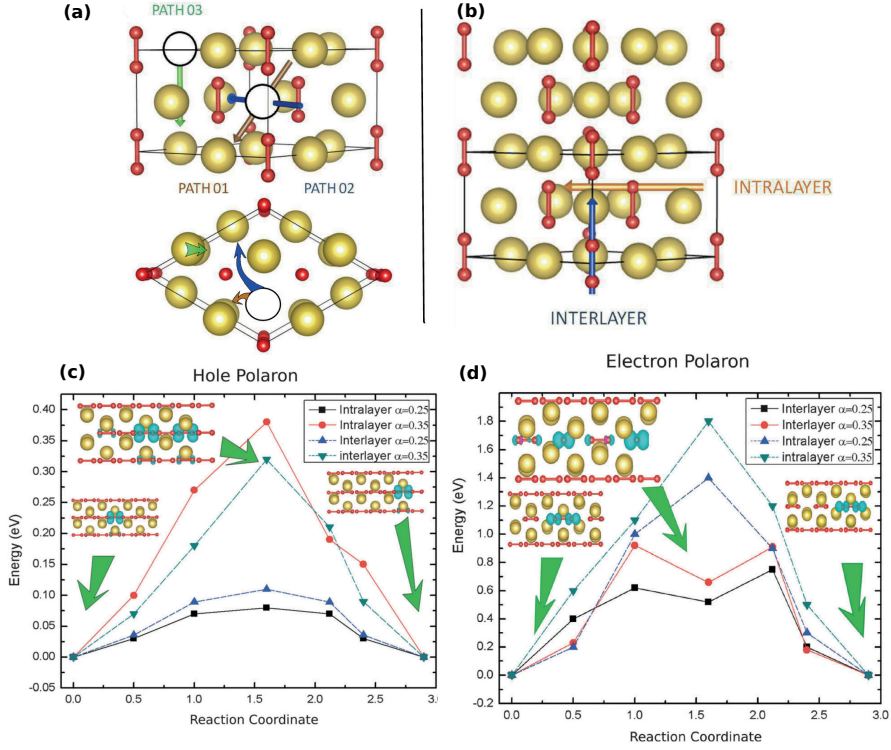


Figure 3.8. (a) Diffusion path for the Na vacancies in the peroxide. (b) Accounted diffusion paths for electron and hole polarons. (c) The activation barriers computed for the hop of polarons in their respective pathways and with different mix parameter for the HSE06 hybrid functional.

tron polaron migration in both pathways. For the intralayer case, the hole polaron activation energy goes from 0.08 eV to 0.38 eV when the amount of exact exchange varies from 25 % to 35 %. For the interlayer path, it undergoes a transformation from 0.11 eV to 0.32 eV for the same mixing parameter variation in the hybrid functional scheme, 25 % to 35 %.

Considering that the charge diffusion will occur through hopping of defects, then the conductivity related to each charge carrier can be derived by the equation:

$$\sigma = \frac{Ce^2a^2v}{k_B T} \exp(-E_a/k_B T) \quad (3.7.3)$$

where C is the defect concentration, k_B is the Boltzmann constant, a^2 is the distance between the hopping sites, v is the related vibrational frequency (10^{-13} Hz) and E_a is the activation energy for the concerned hop. The computation

of this quantity allowed us to conclude that the charge carrier that is primarily responsible for the charge diffusion in Na_2O_2 is the hole polarons. The activation energies of the hole polarons assume values as great as 0.32 eV and 0.38 eV, for the inter- and intralayer paths. It characterizes an anisotropic charge diffusion transport in Na_2O_2 . Moreover, it leads to an intrinsic conductivity value of the order of $10^{-19} \text{ S cm}^{-1}$, which is much greater than the $10^{-2} \text{ S cm}^{-1}$ displayed by the charged vacancy and $10^{-46} \text{ S cm}^{-1}$ for the electron polaron, at room temperature.

4. Thermodynamics of Ions Insertion

The evaluation of the delivered potential of a compound is one of the most important parameters to judge its real application in a battery cell. The potential is directly linked to the electric potential difference displayed by the electrodes. More specifically, in Li-ion batteries, one can say that the potential is a measure of the difference between the chemical potential felt by Li ions in the anode and in the cathode. To get a better perspective of how to compute the delivered potential of a cell, let us evaluate the electric energy delivered by the reaction $\text{Li}_{x_1}\text{H} \rightarrow \text{Li}_{x_2}\text{H}$ where x_1 and x_2 are the lithium contents in the host H. In this case, a Li metal anode is considered with a constant chemical potential of μ_{Li} . Then, the total electric energy delivered will be the integral over all the charge moving from one side (anode) to the other (cathode) and multiplied by the felt potential. It means:

$$E = \int_0^{q_{tot}} V(x) dq \quad (4.0.1)$$

Here, it is assumed that the charge variation is equal to the lithium content variation, $q_{tot} = e(x_1 - x_2)$, and $dq = e dx$. Moreover, the potential is read as $V(x) = -\frac{\mu_{\text{Li}}^{\text{Cathode}}(x) - \mu_{\text{Li}}^{\text{Anode}}}{e}$ leading to:

$$E = - \int_{x_1}^{x_2} \mu_{\text{Li}}^{\text{Cathode}}(x) - \mu_{\text{Li}}^{\text{Anode}} dx \quad (4.0.2)$$

Remembering that the chemical potential is the variation of the Gibbs free energy with respect to the Li content, x , the above integral can be rewritten as:

$$E = - \int_{x_1}^{x_2} \mu_{\text{Li}}^{\text{Cathode}} - \mu_{\text{Li}}^{\text{Anode}} dx = \quad (4.0.3)$$

$$- \left[G_{\text{Li}_{x_2}\text{H}(\text{Cathode})} - G_{\text{Li}_{x_1}\text{H}(\text{Cathode})} - (x_2 - x_1) G_{\text{Li}(\text{Anode})} \right] \quad (4.0.4)$$

$$= -\Delta G \quad (4.0.5)$$

Therefore, the average potential, in volts, can be read as:

$$V = - \frac{\Delta G}{(x_2 - x_1)F} \quad (4.0.6)$$

where, ΔG , is considered as $\Delta G = \Delta E + P\Delta V - T\Delta S$. The contribution of $P\Delta V$ is of the order of 10^{-5} eV per Li atom and $T\Delta S$ contribution is of the order of $k_B T$ at 300 K what is much smaller than ΔE [59]. Therefore, the leading term is the total energy which is directly obtained from the electronic structure calculations.

In order to properly compute the ionic insertion potential in a host material, an accurate description of the crystal structure in each of the x content is required. This is due to the possible structural changes suffered by the material upon the ionic insertion. Most of the algorithms take advantage of the Hellmann-Feynman theorem to seek for the most stable structure, for instance, the conjugate gradient method or quasi-newton scheme. However, these procedures are not able to reach the global minimum in compounds with very complex potential energy surface (PES) or in the cases where the initial structure is far from the global minimum. There exist many algorithms that come up with possible solutions to explore systems with complex PES. In this thesis, the Basin hopping method and an evolutionary scheme were used to investigate structural changes occurred during ionic insertion in some host structures.

4.1 Equilibrium Crystal Structure Prediction

4.1.1 Basin-hopping

The Basin-Hopping algorithm is a method to seek for the global minimum of molecules, clusters and crystals. The method was proposed by David J. Wales et al. [60] and it is based on the idea of transforming the potential energy surface (PES) into interpenetrating local minima forming basins, see Figure 4.1. For this end, an arbitrary initial structure is employed and randomly trial displacements of atoms produce new possible atomic configurations. Then, local structural relaxations are performed for the newly created configuration. Therefore, the total energy related to any point of the configuration space is mapped to that of the local minima computed with the local optimization method. The PES is then transformed into a set of staircases with plateaus correlated to a given minima after local optimization. The total energy change is used to accept or not the new configuration where a Metropolis criteria is applied. The idea behind the acceptance criteria follows: 1. compute ΔE as the total energy difference between the current structure and the newly created, 2. update the old structure to the new structure if $\Delta E < 0$ or if, $\Delta E \geq 0$

and $e^{\frac{-\Delta E}{k_B T}}$ is bigger than a randomly generated number between 0 and 1.

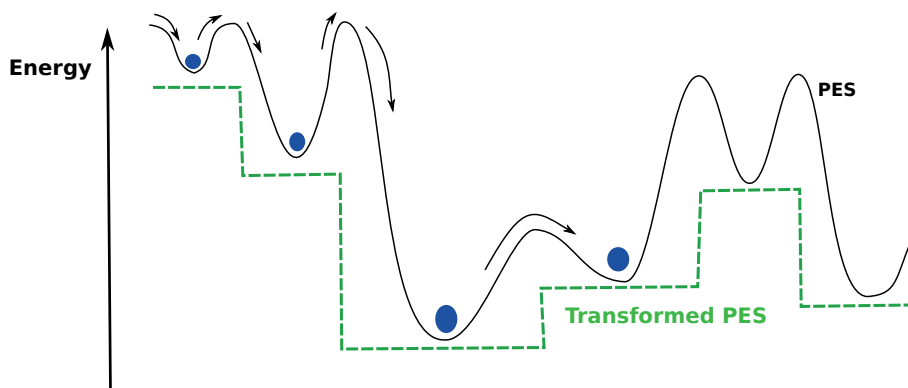


Figure 4.1. Schematic picture showing the basin hopping method. The green lines stand for the transformed PES. The black line represents the real PES

4.1.2 Evolutionary Algorithm

The Universal Structure Predictor: Evolutionary Xtallography (USPEX) [61–63] was employed in this thesis to investigate stable phases (global minimum) of organic compounds with experimental unknown crystal structure. The advantage of employing USPEX in comparison to other methods to locate the global minimum comes from the fact that only the chemical compositions are required. The algorithm employs the Darwinian ideas of natural selection upon the application of variation operators. Its framework follows the steps:

- (1) Randomly generate a set of structures satisfying constraints.
- (2) Applying local optimization methods on the newly generated structures.
- (3) Determine the fittest structures (selection).
- (4) Use the best structures as "parents" of a new generation created by applying variation operators.
- (5) Evaluate the quality of the new structures.
- (6) Repeat 4 and 5 up to a convergence criteria (usually the convergence criteria is when the same structure is repetitively the "best" during a selected number of generations).

The variation operators can be organized into two categories, heredity and mutations. The heredity operator combines two different parents to generate a child. More specifically, the algorithm initially chooses a convenient plane of two structures (parents) and match them. It is important that the number of atoms of the new structure is adjusted to conserve the required number of

atoms. The mutation operators employ small modifications of single parent structure to generate a child. In this case, it can be a lattice mutation, permutation, softmode mutation or rotation mutation. For instance, in the softmode mutation operator, the fractional coordinates are displaced in the direction of the soft mode eigenvectors or a linear combination of them and the permutation operator randomly swaps pairs of distinct atomic species.

The seek for the most stable crystal structure of organic compounds presents some important features in comparison to the case of inorganic compounds. These are: i) Large volume unit cells are observed for organic materials with a higher amount of atoms. ii) High distances between the molecules leading to great empty spaces in the structure. iii) The necessity of fixing intramolecular connectivity. iv) Uneven distribution of structures over symmetry groups (most of the organic materials displays space groups: $P2_1/c$, $P-1$, $P2_12_12_1$, $C2/c$, $P2_1$ and $Pbca$ [64]). Points number i) and ii) indicate a large search space that randomly would, in most of the cases, explore regions out of interest. On the other hand iii) and iv) help with these issues. Indeed, the global optimization is performed with a restriction of fixed intramolecular connectivity, otherwise, the molecules could combine forming distinct compounds that are not the main target. From iv), it is observed that the selection of most probable symmetries in the random search can also improve the efficiency of the algorithm diminishing the search space.

4.2 Case 01: Ionic Insertion in $\text{Na}_x\text{Fe}(\text{SO}_4)_2$

Recently, P. Singh et al. [65] reported a low-cost cathode material, eldfeelite ($\text{NaFe}(\text{SO}_4)_2$), with reversible sodium insertion capability at a voltage of 3.2 V vs. Na/Na^+ , for the $\text{Fe}^{3+}/\text{Fe}^{2+}$ redox activity. This compound comes with a moderate specific energy and issues regarding the ionic insertion rate. However, it is possible to implement structural changes able to tune the actual specific energy. This could be done by allowing a two electron reaction with full Na removal from the host. The crystal structure of this compound is depicted in Figure 4.2 (a). The initial step of the investigation is to study the main battery reaction, $2\text{Na}^+ + 2\text{e}^- + \text{Fe}(\text{SO}_4)_2 \rightarrow \text{Na}_2\text{Fe}(\text{SO}_4)_2$. It is important for this task to find the global minimum configurations of the compounds $\text{Na}_x\text{Fe}(\text{SO}_4)_2$, with x varying from 0 to 2. From the experiment, the fractional position of the Na ions into the eldfeelite crystal structure with $x=1$ is already known. However, the Na fractional coordinates for the compounds with Na concentration different of $x=1$ are unknown. Hence, to further investigate such reaction, it is important to apply a global minimization method able to identify the ground state structure for the compounds with each Na content. The basin hopping algorithm was employed to find out the global minimum structure. The method has been adapted to only randomly modify the position of Na atoms in the used supercell. Then, the crystal structure of

the host, $\text{Fe}(\text{SO}_4)_2$, undergoes only the local energy minimization procedure. Figure 4.2 (a) shows the two fractional positions where Na atoms are placed. The compounds with Na concentrations lower than $x=1$ must have the sodium ions populating Na1 positions. Then, for x going from 1 to 2, the sodium ions must assume the Na2 positions. Once the global minimum structure of each x

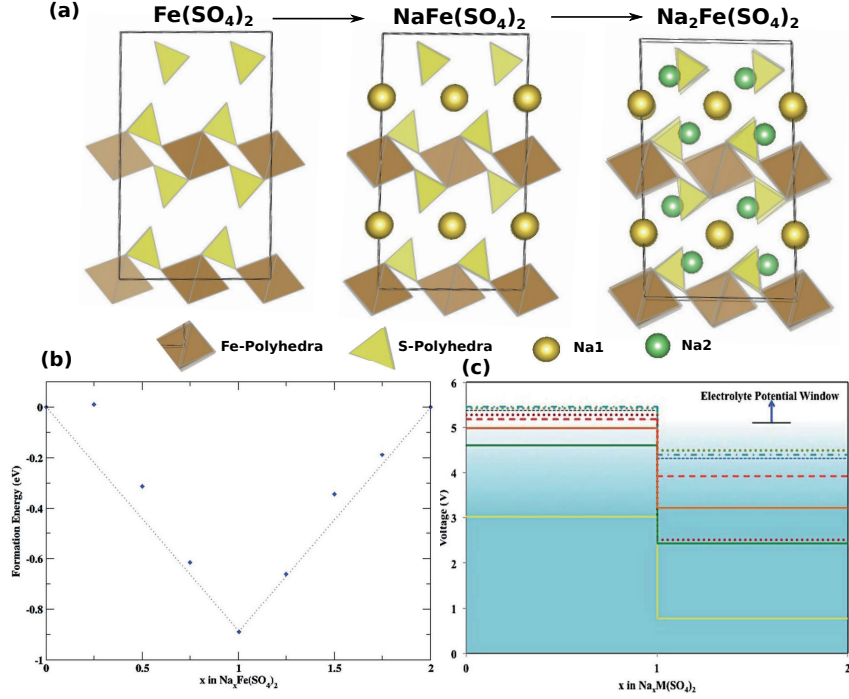


Figure 4.2. (a) Crystal structure of $\text{Fe}(\text{SO}_4)_2$, $\text{NaFe}(\text{SO}_4)_2$ and $\text{Na}_2\text{Fe}(\text{SO}_4)_2$. (b) Formation energy vs. the Na content into the host compound. (c) Delivered voltage for the $\text{Na}_2\text{Fe}(\text{SO}_4)_2$ with Fe substituted by other transition metal atoms.

composition was identified by checking hundreds of different sodium configurations, the formation energies of these compounds are calculated with respect to two end structures, i.e., $\text{Fe}(\text{SO}_4)_2$ and $\text{Na}_2\text{Fe}(\text{SO}_4)_2$, by the following equation and represented in Figure 4.2 (b):

$$E_f = E_{\text{Na}_x\text{Fe}(\text{SO}_4)_2} - \left[\frac{x E_{\text{Na}_2\text{Fe}(\text{SO}_4)_2} + (2-x) E_{\text{Fe}(\text{SO}_4)_2}}{2} \right] \quad (4.2.1)$$

Only three Na-ordered phases appear in the tie-lines of the convex hull, $x=0$, 1 and 2. Any other concentration is higher in energy than the linear combination of the concerning concentrations during the Na insertion reaction. Thus, the potential profile of the Na insertion can be extracted from the

compositions lying on the convex hull line and computed by the equation:

$$V = - \left[\frac{E_{Na_xFe(SO_4)_2} - (x - x_0)E_{Na(bcc)} - E_{Na_{x_0}Fe(SO_4)_2}}{(x - x_0)} \right] \quad (4.2.2)$$

where x stands for the Na concentration in the host. For example, the first step reaction, $Na^+ + e^- + Fe(SO_4)_2 \rightarrow NaFe(SO_4)_2$, x_0 goes to 0 and x amounts to 1. The computation of the voltage profile is depicted in Figure 4.2 (c). It is obtained two voltage plateaus. The first case displays a value of 4.98 V vs. Na/Na^+ , what is very close to the potential window of currently used electrolytes. The second voltage plateau reaches 3.2 V vs. Na/Na^+ what is in agreement with the experimental measurement, 3.2 V vs. Na/Na^+ [65]. Due to the high potential of the first plateau, 4.98 V vs. Na/Na^+ , it is unlikely to achieve the extraction of both Na atoms from this polyanion when conventional electrolytes are employed.

One possible strategy to overcome this issue is, therefore, to substitute the used transition metal, Fe, by compounds presenting slightly lower voltage. This strategy was employed by substituting Fe by Co, Cr, Cu, Mn, Ni, Ti and V. The computed sodium insertion potential for the substituted compounds are also depicted in Figure 4.2 (c). A close analysis of the potential profiles reveals the substitution of Fe by Ti or V as the best options. This is due to the delivered redox potential values shown by these materials with the first plateau lower than 5 V vs. Na/Na^+ . On the other hand, the Ti-based system emerges with a quite lower potential for the second plateau producing lower specific energy when this transition metal is employed. Therefore, V substitution is the most promising modification to reach the two electron reaction. This compound must produce a theoretical specific energy of the order of 689 Wh/kg, which is higher than the value presented by the currently used cathode $LiFePO_4$ (440 Wh/kg).

4.3 Case 02: $C_6Cl_4O_2$ as an Organic Cathode of Sodium Batteries

$C_6Cl_4O_2$ has recently been proposed by Haegyeom et al. [66] as an alternative for the application as a cathode of advanced sodium batteries. This compound is a modification of the p-benzoquinone with electron-withdrawing substitutions to deliver greater potentials. The experiment reveals a potential profile with two main plateaus, one at 2.6 V vs. Na/Na^+ and the other at 2.9 V vs. Na/Na^+ . These plateaus lead to an average deintercalation potential reaching to a value as high as 2.72 V vs. Na/Na^+ , what is comparable to the delivered potential displayed by inorganic materials as the cathode of sodium batteries. Moreover, $C_6Cl_4O_2$ emerges as the organic material with higher delivered potential already reported vs. Na/Na^+ [66].

Table 4.1. Experimental lattice parameters from Ref. [67] as well as the predicted lattice parameters considering the distinct schemes to treat the exchange and correlation term of the Kohn-Sham Hamiltonian. The values in parenthesis are the difference concerning the experimental value in percentage.

	Exp.	PBE	PBE+D2	HSE06 (25 %)	HSE06 (55%)
a (Å)	8.67	9.52 (9.8 %)	8.93(2.7 %)	9.32(7.2 %)	8.79(1.3%)
b (Å)	5.68	6.16 (8.4 %)	5.66(-0.3 %)	5.94(4.5 %)	5.91(3.8 %)
c (Å)	8.54	9.15 (7.1 %)	8.70(1.7 %)	8.82(3.2 %)	8.58(0.4 %)
α	90.00	90.00	90.00	89.99	89.99
β	105.94	109.00	106.71	108.09	106.68
γ	90.00	89.99	89.99	90.02	90.00
Volume (Å ³)	405.14	507.22(25 %)	421.79(4 %)	465.02(15 %)	428.19(6 %)

The initial goal of this investigation is to employ the framework of the evolutionary simulation together with the density functional theory formalism to unveil the structural changes experienced by $\text{C}_6\text{Cl}_4\text{O}_2$ during the electrochemical reaction. The knowledge of the ground state structures of the compounds $\text{Na}_x\text{C}_6\text{Cl}_4\text{O}_2$, with x going from 0 to 2, must enable us to better understand the driven factors behind the battery reaction. Once the crystal structures are determined, the hybrid functional method is employed to investigate the electronic structure of the chloranil with distinct Na content. The thermodynamics analysis of the battery reaction showed an unlikely process for the Na insertion after the formation of the compound $\text{Na}_{1.5}\text{C}_6\text{Cl}_4\text{O}_2$, in agreement with the experimental observations. Finally, the observed two plateau in the potential profile is properly explained by the electronic structure analysis.

4.3.1 The Crystal Structure Search

The chloranil crystal structures, at 150 K, stabilizes in a monoclinic phase with space group $P2_1/a$ and lattice parameters as summarized in Table 4.1. The crystal unit cell shows two crystallographic non-equivalent molecules, as depicted in Figure 4.3 (a). Table 4.1 summarizes the obtained lattice parameters coming from the evolutionary simulation and the local energy minimization from DFT. A great discrepancy was observed regarding the experimental lattice parameters and the value predicted within PBE functional. This trend indicates the necessity to properly treat the long range dispersion interactions. With the inclusion of the dispersion, as suggested by Grimme (PBE+D2), the obtained results have greatly improved yielding a volume difference of only 4 %, when compared to the experimental data.

To overcome the self-interaction error and correctly describe the electronic structures of the referent material, the HSE06 hybrid functional was also employed. This strategy brought remarkable improvements in the structural description when 55 % of exact exchange was applied, as shown in Table 4.3.1. Even without properly treating the dispersion interactions, this method itself

commits excellent agreement with the experimental data. It is also worth to highlight that this amount of exchange reproduced the computed GW_0 band gap of 4 eV revealed by the chloranil.

The Na insertion into the $\text{C}_6\text{Cl}_4\text{O}_2$ host is followed by great distortions of the crystal unit cell. Figure 4.3 shows the ground state crystal structures found by the evolutionary simulation for the compounds $\text{Na}_x\text{C}_6\text{Cl}_4\text{O}_2$, with $x=0.5$, 1.0, 1.5 and 2.0. The simulations have shown the formation of salt regions formed of Na-O bounded by shared O atoms with the $\text{C}_6\text{Cl}_4\text{O}_2$ units. The formation of these regions, under Na insertion, occurs mostly through rotation of chloranil molecules. The structural stability of the predicted systems, $\text{Na}_x\text{C}_6\text{Cl}_4\text{O}_2$, with $x=0.5$, 1.0, 1.5 and 2.0, were evaluated in terms of formation energy using the following equation:

$$E_f = E(\text{Na}_x\text{C}_6\text{Cl}_4\text{O}_2) - \frac{[xE(\text{Na}_2\text{C}_6\text{Cl}_4\text{O}_2) + (2-x)E(\text{C}_6\text{Cl}_4\text{O}_2)]}{2} \quad (4.3.1)$$

where E stands for the total energy of the compound in parenthesis.

Figure 4.4 displays the formation energies computed with PBE and PBE+D2 schemes. The compound with $x=0.5$ appears in the tie-line of the convex hull for the PBE+D2 picture and out of the tie-line for the pure PBE, but with a small energy distance from the line of the convex hull. The compound with $x=1$ emerged as a stable phase for both methods. Finally, the linear combination of the compositions with $x=1$ and $x=2$ showed to be more energetically favorable than the case of $x=1.5$ for both functional. The formation energies, depicted in Figure 4.4 (b), emerge with another feature. The HSE06 scheme, with different amount of exact exchange, has shown the bottom of the hull in a distinct position if compared with the PBE and PBE+D2 methods. Furthermore, it displays the case of $x=0.5$ out of the convex hull line while the other considered compositions showed favorable formation energies.

4.3.2 The Ionic Insertion Potential and Capacity

The evaluation of the potential profile is represented in Figure 4.5. The calculations considered only the compositions lying on the tie-line of the convex-hull. The results were in quite good agreement with the reported experimental data [66]. The trend of two voltage plateaus upon the cell discharge was well reproduced by theoretical predictions in the different exchange and correlation flavors. The first step of the reaction, with x going from $x=0$ to $x=1$, corresponded to a potential of 2.9 V vs. Na/Na^+ . The calculated values varied from 2.88 V to 3.11 V vs. Na/Na^+ depending on the used methodology. This leads to a maximum discrepancy of 7 % for HSE06 with 55 % of exact exchange and less than 1 % when PBE functional is employed.

The second voltage plateau showed a potential of 2.6 V vs. Na/Na^+ in the experiment. The predicted potential profile reproduced this value with a discrepancy of around 9.6 % when the pure PBE result is employed. The addition of

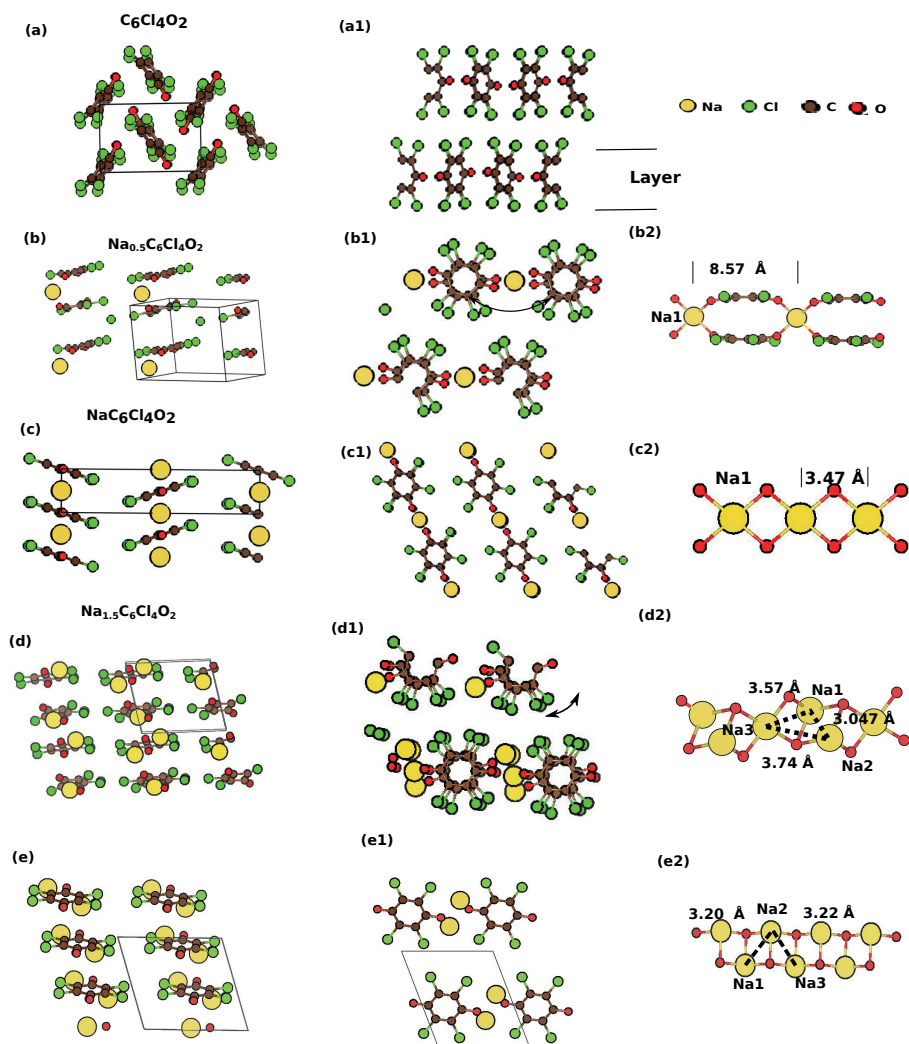


Figure 4.3. Representative picture of the experimental crystal structure of chloranil (a) together with the most stable phases found from the evolutionary simulation for the compounds (b) $Na_{0.5}C_6Cl_4O_2$, (c) $NaC_6Cl_4O_2$, (d) $Na_{1.5}C_6Cl_4O_2$ and (e) $Na_2C_6Cl_4O_2$. Here, the yellow, red, green, and brown balls represent respectively, Na atoms, O atoms, Cl atoms and C atoms. First two columns of the figure depict different orientations. The last column presents the changes in the Na-O bonds upon sodium insertion. The bond distances in this picture were computed within PBE-D2 approach.

the long-range interactions, within the PBE+D2 method, should emerge with better results since it can properly describe the related structural properties. However, no real improvement is obtained for the computation of the seconde plateau with this method. A similar result is also reported by T. Yamashita et al. [68]. Following the same trend, the HSE06 functional yielded higher discrepancies than the PBE. On the other hand, the inclusion of a percentage of exact exchange in the calculation induced the Na insertion to a maximum concentration of $x=1.5$ (since the insertion potential revealed a negative value for x going from 1.5 to 2). This result was in really good agreement with the experimental measurements, which prescribes a maximum reversible Na concentration of $x=1.42$ during the cell reaction [66].

In summary, it was shown that good predictions of the ionic insertion potential can be obtained at the PBE level of theory. This method is less computationally time consuming than the hybrid functional scheme and it could come up with accurate redox potentials. On the other hand, the application of the HSE06 functional was essential to correctly predict the maximum specific capacity of the $C_6Cl_4O_2$ cathode.

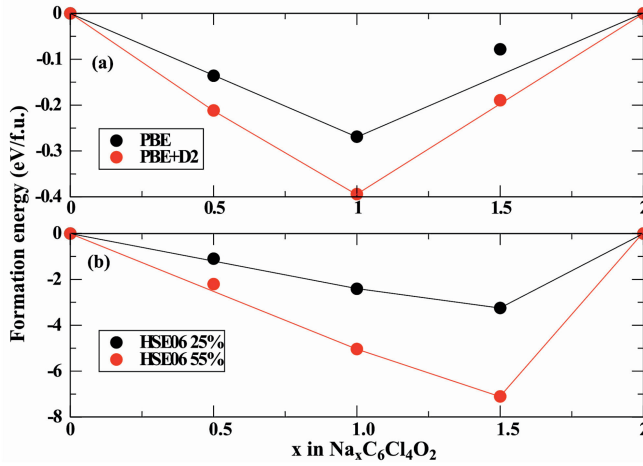


Figure 4.4. Formation energy as a function of x in eV/f.u. with: (a) PBE and PBE+D2. (b) HSE06 with 25 % of exact exchange and HSE06 with 55 % of exact exchange. The formation energies were computed considering the ground state structures found in the evolutionary simulation.

4.4 Case 03: 2D compounds as the anode of rechargeable batteries

In the recent years, 2D compounds have found their place in the application as an anode of rechargeable batteries. This is due to advantages such as their

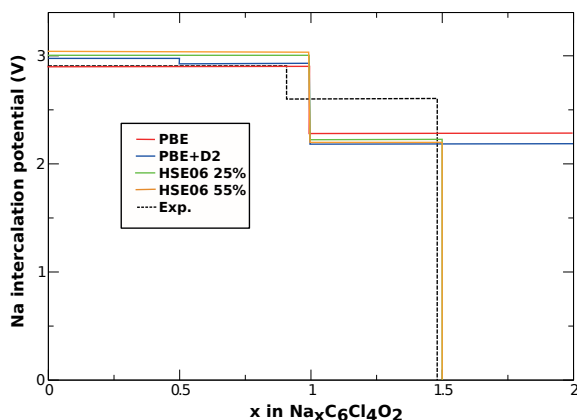


Figure 4.5. Calculated voltage profile of $\text{Na}_x\text{C}_6\text{Cl}_4\text{O}_2$ vs. Na/Na^+ for x varying from 0 to 2. The dashed line represents the experimental values of 2.9 V and 2.6 V vs. Na/Na^+ [66]. Red line is the calculations with PBE, the blue line represents the calculations with PBE+D2, the green line is the calculations with HSE06 with 25 % of exact exchange and orange is the HSE06 with 55 %.

higher electronic surface area, remarkably high electron mobility and superior mechanical properties [69]. Moreover, their unique morphology enables greater power densities as a result of the low activation barriers felt by the ionic migration. In this thesis, two materials were investigated, by means of the density functional theory, as alternative anodes for state-of-art batteries, as presented in the following sections.

4.4.1 The 2D- B_2H_2 anode

Borophene was first proposed as a 2D compound by Mannix et al. [70]. He has reported the formation of 2D elemental boron in a silver surface. The main issue revealed by the borophene concerns its stability since the growth of it is achieved only on metal surfaces. Motivated by this experiment, Xu et al. [71] used the DFT framework to show that complete surface hydrogenation of borophene provides a path into a stable material named borophane. Since then, many applications of this compound have been reported in fields such as microelectromechanical devices [72] and sensing properties [73]. Figure 4.6 (a) represents the structure of this material. It is revealed a buckling height of 0.84 Å and B–H bond distance of 1.18 Å. Moreover, the computed band structure of this material showed characteristic Dirac cone between Γ to X directions.

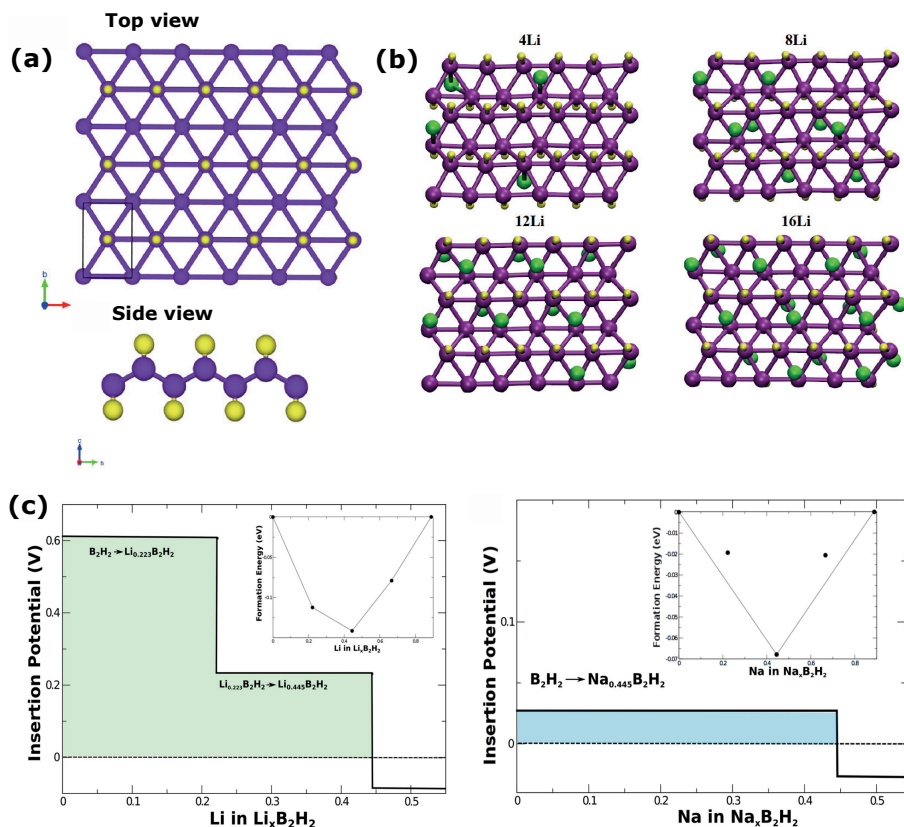


Figure 4.6. (a) Top and side view of B_2H_2 . (b) Top view of $Li_xB_2H_2$. Potential profile of the Li and Na adsorption in the borophane surface.

The analysis of B_2H_2 as an anode material starts with the investigation of the Li/Na absorption on the borophane surface by employing the global minimum structures obtained from the swapping basin hopping algorithm. The relaxed structures correspond to the adsorption of 4, 8, 12, and 16 Li/Na atoms ($x = 0.223, 0.445, 0.667$, and 0.889 with x in $Li/Na_xB_2H_2$) and the case of Li is presented in Figure 4.6 (b). The access of these structures allowed the calculation of the Li/Na adsorption potential profiles and the results were plotted in Figure 4.6 (c). We have shown that for both counter ions the maximum allowed adsorption concentration goes to $x=0.44$ per formula unity. The main difference among Li and Na cases is the appearance of two plateaus in the Li potential profile with values of 0.61 V and 0.23 V vs. Li/Li^+ and a single plateau for the Na case with 0.03 V vs. Na/Na^+ . That ionic concentration gives rise to a theoretical specific capacity of 504 mAh/g for Li and Na which

is in the range of currently investigated 2D compounds for an anode application [74–77].

4.4.2 The 2D-Si₂BN anode

Andriotis et al. [78] have firstly proposed 2D-Si₂BN employing the DFT framework. He showed the structural and thermal stability of this material by means of phonon dispersion calculations as well as molecular dynamics simulation. Figure 4.7 shows the Si₂BN structure. From the electronic structure calculation, it was shown that there is band crossing at the Fermi level resulting in a metallic compound. Considering the specific application as the anode of an advanced battery, the metallic behavior emerges as an advantage, moreover, the existence of Si-Si bonds could work as a redox center and serving as electrons reservoir. Therefore, the general properties of this compound indicate that it could be a good alternative for such application.

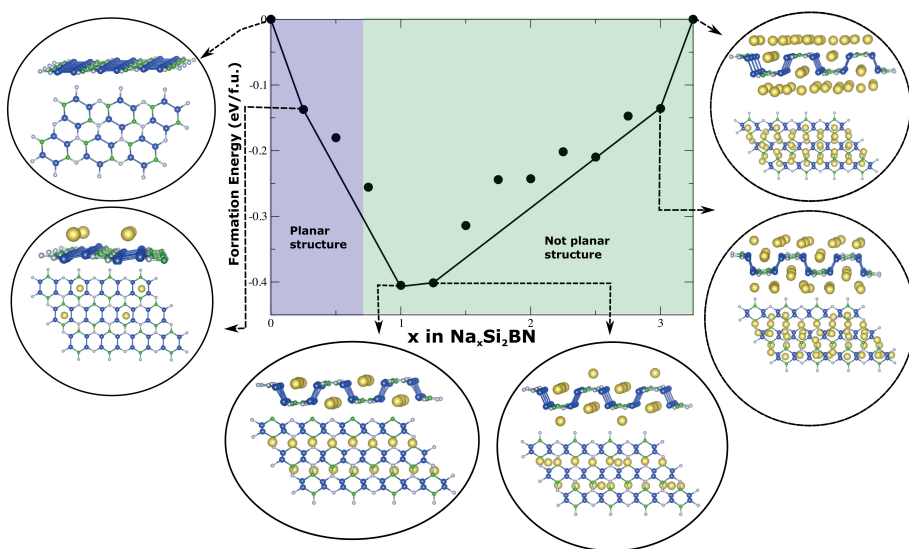


Figure 4.7. Formation energies of the compounds Na_xSi₂BN as a function of x in eV/f.u. The formation energies were computed considering the ground state structures obtained by the basin hopping algorithm. The found structures lying in the tie-line of the convex hull are depicted

The investigation of the ionic potential adsorption of Li/Na in the Si₂BN surface starts by finding out the global minimum structures for each ionic content. In this case, we have considered ionic concentrations, x in Li/Na_xSi₂BN, varying from 0 to 3.50, for the Li case, and from 0 to 3.25, for the Na case.

The computation of the internal energy of these structures has permitted the analysis of their stability through the plot of the convex hull. Phases appearing in the tie line of the convex hull must actually exist during the reaction. On the other hand, the structures out of the tie line must disproportionate forming a two phase electrode. Therefore, the computation of the adsorption potential considers only phases lying in the tie-line of the hull, as shown in Figure 4.7 for the Na case. We have shown that this material undergoes a structural transformation from a layered structure to a puckered one upon the insertion of one Li/Na per formula unit at potentials of 0.67 V vs. Li/Li^+ for Li adsorption and 0.60 V vs. Na/Na^+ for Na adsorption. We could speculate that the filling of antibonding states creates some level of stress in the structure leading to a puckered phase. The final ionic concentration, the one that comes with a negative voltage or undergoes irreversible structural changes, amounts to $x=3.5$ for Li and 3.0 to Na at potentials of 0.34 V vs. Li/Li^+ and 0.09 V for Na/Na^+ , respectively. This leads to theoretical capacities as high as 1158 mAh/g and 1076 mAh/g for the Li based device and the Na based device.

5. Electronic Structure and Charge Disproportionation Analysis

As discussed in previous chapters, the ionic insertion into a compound, employed as the electrode of a rechargeable battery, is followed by a reduction reaction procedure. For instance, the battery reaction $\text{Na}^+ + \text{e}^- + \text{NaFe}(\text{SO}_4)_2 \rightarrow \text{Na}_2\text{Fe}(\text{SO}_4)_2$ comes with an insertion potential of the order of 3.2 V vs. Na/Na^+ concerning the redox pair $\text{Fe}^{2+}/\text{Fe}^{3+}$. It means that the extra electrons donated by the Na atoms must populate *d* orbitals of Fe centers. For the specific case, it is easy to attribute the reduction center to the transition metal. However, there are many situations where the redox center is not so clear. For example, Hungru Che et al. [79] showed that Li insertion and removal in MnO_3 is charged compensated by the oxygen sublattice. In this thesis two main strategies were employed to investigate charge compensation and electron localization. One is the electronic structure analysis. As expected, the addition of an extra pair Na^+ and e^- in the host compound is followed by changes in the electronic structure of the referent material. This kind of effect can be observed in the projected density of states (PDOS) by specific fingerprints. One of them is related to the atomic contribution for the DOS in the vicinity of the Fermi level and in the bottom of the conduction band. These are the states that actively participate in the redox reaction. Thus, the atoms with a greater contribution in this region should be the ones experimenting the charge compensation with the ionic removal/insertion. Another fingerprint commonly observed is change in the local magnetic moment of some atoms, such as the Fe case with the redox process. The second strategy is to use the Bader charge analysis. The main idea behind this method is to integrate the charge density within a surface with specific characteristics and to assign the resulted charge to an atom in the crystal [80–82]. With this strategy, one can compute the Bader charges of a host compound before and after the redox reaction and compare the values. It would give some insight of the active redox centers and the electron localization.

5.1 Case 01: $\text{Nb}_2\text{O}_2\text{F}_3$

The recently synthesized crystal structure of $\text{Nb}_2\text{O}_2\text{F}_3$ [83] consists of NbX_6 ($\text{X} = \text{O}$ or F) octahedra sharing edges of X and then forming Nb_2X_{10} dimers. The dimers are linked by sharing X atoms along the *c* direction forming a kind

of layered structure. The structure stabilizes in a monoclinic I2/a space group with a possible phase transition at 90 k to a triclinic, P1, structure. This opened framework allows the insertion of Li atoms and, then, it could be employed as the electrode of rechargeable batteries, as shown in Figure 5.1 (a-c).

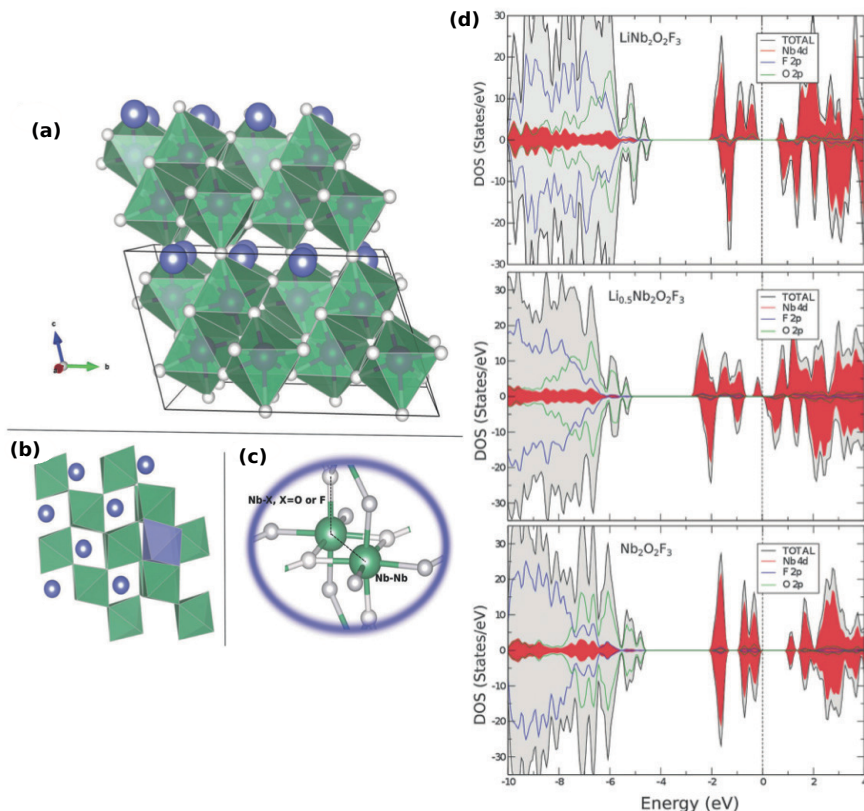


Figure 5.1. (a) Crystal structure of $\text{LiNb}_2\text{O}_2\text{F}_3$. Here, the green color octahedra represent Nb_2X_{10} ($\text{X} = \text{O}, \text{F}$) dimers. White balls are O or F atoms. Blue balls are Li atoms. (b) Top view of $\text{LiNb}_2\text{O}_2\text{F}_3$. The blue octahedra LiX_6 represents the position where the ions are placed. (c) A closer look at the Nb_2X_{10} dimer structure. There, it is possible to see the Nb–Nb bond and also the Nb–X bond. (d) Total and projected density of state (pDOS) evaluated for $\text{LiNb}_2\text{O}_2\text{F}_3$, $\text{Li}_{0.5}\text{Nb}_2\text{O}_2\text{F}_3$ and $\text{Nb}_2\text{O}_2\text{F}_3$. Gray color represents the total DOS, red color represents d states of Nb atoms summed up, blue lines represent p states of F atoms summed up and green lines represent p states of O atoms summed up.

Figure 5.1 (d) depicts projected and total density of states (pDOS and DOS) of the lithiated and delithiated compounds. The presented results are in complete accordance with the current trend of battery materials [84] where *d* states of transition metals dominate around the valence band maximum (VBM) and

the conduction band minimum (CBM). It is also worth emphasizing that the lithiation process in this system comes with a semiconductor to metal transition when half of the Li atoms are inserted and, then, the semiconductor behavior is recovered when the other half lithium atoms are included. By considering a molecular orbital picture of Nb–Nb bonds, t_{2g} orbitals coming from Nb–4d states would hybridize forming $\sigma^2\pi^1$ filled molecular orbitals (MOs) [83]. Hence, the insertion of half Li atoms leads to a charge rearrangement where half of the Nb–Nb have filled π^2 states while the other half Nb–Nb part presents the π^1 . The population of the π^2 states is followed by a symmetry break of the system and, then, a transition from semiconductor to metal is obtained, as shown by the pDOS. Further, the insertion of other 0.5 Li atom per formula unit recovers the symmetry of the system and also the metal behavior.

The Bader analysis method is employed to further understand charge rearrangement over Li insertion. Nb atoms in the delithiated state present an average net charge of +2.34. With the addition of Li atoms in the crystal structure of Nb₂O₂F₃ forming LiNb₂O₂F₃ the value goes to +2.02. It means that each pair Nb–Nb undergoes a reduction process receiving approximately one electron. The average net charge change of O and F atoms displays very small values amounting to +0.04 and +0.06 under lithiation. This result is in accordance with the structural analysis where Nb–Nb bond distances decrease with Li ion insertion whereas the Nb–X bond length remains almost the same value (not participating in the reaction).

5.2 Case 02: Na₂M₂(SO₄)₃ with M=Fe, Mn, Co and Ni

Recently, the alluaudite structure compounds, Na₂M₂(SO₄)₃ with M=Fe, Mn, Co, Ni, based on Fe and Mn has been proposed as a promising cathode material for sodium batteries [55, 85]. This is owed to their very high redox potential vs. Na/Na⁺ as well as reasonable reaction rate. One strategy to improve the energy density in the alluaudite family can be achieved by substituting the currently used transition metals in the cathode polyanion by Co or Ni atoms. However, each choice of transition metal comes along with their respective properties. To gain a profound understanding of the electrochemical properties of Na₂M₂(SO₄)₃ (M = Fe, Mn, Co and Ni) based electrodes, it is important to study the charge transfer process upon the ionic insertion for each case. Therefore, the average net charge per atom has been computed for all cases and compared. Here, the average net charge is defined as the charge calculated with the Bader analysis minus the total nuclear charge of the related atomic species. Table 5.1 summarizes the results of the average Bader charge for the considered compounds.

For the whole series of Na₂M₂(SO₄)₃ (M = Fe, Mn, Co and Ni) compounds, the Bader charges are very similar for sodium, sulfur and oxygen units, amounting to an average of +0.85 for the sodium case and ranging from

Table 5.1. Average Bader charge of the ground state of $\text{Na}_2\text{M}_2(\text{SO}_4)_3$, $\text{NaM}_2(\text{SO}_4)_3$ and $\text{M}_2(\text{SO}_4)_3$ ($\text{M}=\text{Fe}, \text{Mn}, \text{Co}$ and Ni).

Compound	Na	M	S	O
$\text{Na}_2\text{Fe}_2(\text{SO}_4)_3$	+0.85	+1.49	+3.87	-1.36
$\text{NaFe}_2(\text{SO}_4)_3$	+0.85	+1.67	+3.87	-1.34
$\text{Fe}_2(\text{SO}_4)_3$	–	+1.85	+3.86	-1.30
$\text{Na}_2\text{Mn}_2(\text{SO}_4)_3$	+0.85	+1.56	+3.87	-1.37
$\text{NaMn}_2(\text{SO}_4)_3$	+0.85	+1.65	+3.87	-1.32
$\text{Mn}_2(\text{SO}_4)_3$	–	+1.78	+3.88	-1.27
$\text{Na}_2\text{Co}_2(\text{SO}_4)_3$	+0.85	+1.43	+3.80	-1.32
$\text{NaCo}_2(\text{SO}_4)_3$	+0.85	+1.46	+3.81	-1.26
$\text{Co}_2(\text{SO}_4)_3$	–	+1.51	+3.88	-1.22
$\text{Na}_2\text{Ni}_2(\text{SO}_4)_3$	+0.85	+1.37	+3.85	-1.32
$\text{NaNi}_2(\text{SO}_4)_3$	+0.85	+1.37	+3.85	-1.26
$\text{Ni}_2(\text{SO}_4)_3$	–	+1.37	+3.85	-1.11

+3.80 up to +3.85 and -1.32 to -1.36 for sulfur and oxygen, respectively. Considering the total ionic bond picture, oxygen atoms should display a -2 atomic charge. However, the hybridization effects cause the effective charge of the O centers to be around -1.32 , and that for S atoms to be around +3.85. For the transition metal series, the average charge values amount to +1.49, +1.56, +1.43 and +1.37 for Fe, Mn, Co and Ni, respectively.

After the removal of half the sodium ions from the fully sodiated structure, an unexpected trend is obtained for the polyanions containing Co and Ni as the transition metal. The computed Bader charges for $\text{NaCo}_2(\text{SO}_4)_3$ and $\text{NaNi}_2(\text{SO}_4)_3$ present almost no change for the cobalt case and, in fact, no change for the Ni case. It means that the oxidation reaction under sodium removal is likely taking place in the oxygen sublattice. For instance, the full desodiation of the polyanion with Ni results in an average Bader charge in the oxygen ions of -1.11 , against -1.32 for the fully sodiated case. This difference, multiplied by the number of O atoms in the unit cell, produces a value close to 8, which is the number of lost electrons during the electrochemical reaction per unit cell. Therefore, the O anionic sub-lattice appears to be the responsible for the net oxidation process during the desodiation reaction.

6. Theory to Predict Redox Potential in Solution

The main objective of this chapter is to present the employed computational method to compute the standard reduction potential of a redox reaction in solution. The standard reduction potential can be obtained by using the Nernst equation:

$$E^0 = -\frac{\Delta G_{(solv)}(Red)}{nF}, \quad (6.0.1)$$

where n stands for the number of electrons participating in the reaction and F is the Faraday constant. The computation of $\Delta G_{(solv)}(Red)$ is performed on the basis of the Born-Haber thermodynamic cycle displayed in Scheme 6.1. Therefore, $\Delta G_{(solv)}^{(Red)}$ can be expressed as:

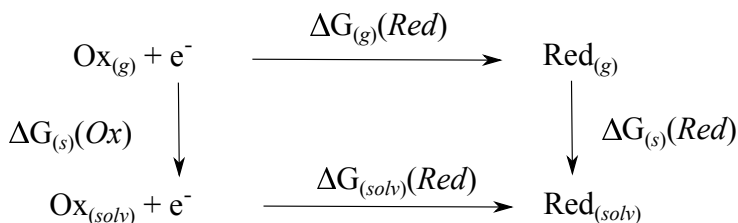


Figure 6.1. Born Haber thermodynamic cycle.

$$\Delta G_{(solv)}(Red) = \Delta G_{(g)}(Red) + \Delta G_{(s)}(Red) - \Delta G_{(s)}(Ox) \quad (6.0.2)$$

where $\Delta G_{(g)}(Red)$ is the Gibbs free energy in gas-phase, $\Delta G_{(s)}(Red)$ and $\Delta G_{(s)}(Ox)$ are the solvation free energy of the reduced and oxidized species, respectively. G was evaluated with the density functional theory framework as:

$$G = U + PV - T(S_{vib} + S_{rot} + S_{trans}) \quad (6.0.3)$$

and

$$U = ZPE + E_{ele} + U_{vib} + U_{trans} + U_{rot}. \quad (6.0.4)$$

where ZPE is the vibrational zero point energy, E_{ele} is the electronic energy, U_{vib} , U_{rot} and U_{trans} are the vibrational, rotational and translational energies and S_{vib} , S_{rot} and S_{trans} are the respective entropic effects.

The evaluation of $\Delta G_{(solv)}(Red)$ and $\Delta G_{(solv)}(Ox)$ have employed an implicit solvation model, where the solvent is represented by a continuum and polarized medium with dielectric constant ϵ instead of explicitly including the solvent molecules in the calculations [86]. This process starts by creating a cavity region that must accommodate the solute into the solvent. In most of the cases, this cavity is a superposition of atomic centered spheres where the radio of the spheres is dependent of the atomic species. Inside this region, the dielectric function assumes the value of 1, as in vacuum. Then, the solvation free energy can be read as the necessary work to create the cavity plus all the reorganization effects related to the interaction of the solute with the polarized medium, as represented by the following equation:

$$\Delta G_{(solv)} = \Delta G_{(Ele)} + \Delta G_{(Cav)}. \quad (6.0.5)$$

Here, $\Delta G_{(Cav)}$ stands for the formation energy of the cavity as stated before. $\Delta G_{(Ele)}$ accounts to the changes in the electronic structure of the solute and the electric polarization of the medium upon the insertion of the solute into the solvent. Therefore, $\Delta G_{(Ele)}$ can be written as:

$$\Delta G_{(ele)} = \langle \Psi_s | \varphi_d | \Psi_s \rangle + \Delta E_p. \quad (6.0.6)$$

In this case, ΔE_p concerns the change of the electronic cloud upon insertion of the molecule in the medium. Ψ_s is the system wave function in solution and φ_d is the electrostatic potential due to the polarized medium. The first term in eq. 6.0.6 accounts to the interactions of the polarization's charges of the medium with each electron and the nuclei of the solute. φ_d is assessed by solving the Poisson's equation [86, 87] using the Poisson-Boltzmann self consistent field (PBF) solver [88, 89] as implemented in the JAGUAR code [90, 91]. In summary, the procedure to model a molecule in solution by means of the continuum model is: Firstly, it is computed the gas phase wave function of the current compound. From that, an electrostatic potential is derived for vacuum and fits it to a charge distribution. Secondly, this charge density is introduced in the Poisson-Boltzmann solver that uses finite differences method to get the electrostatic potential for the dielectric constant of the medium and to represent the solvent as a layer of charges at the cavity surface. Then, another wave function is computed with Jaguar by including the effects of the solvent charges. This process is then repeated self consistently up to a convergence parameter.

In this thesis, all calculations were performed considering a continuum medium mimicking the CH₃CN (acetonitrile) solvent with the dielectric constant of $\epsilon = 37.5$ and solvent radius of 2.19 Å. Moreover, the temperature effects were set to a value of 298 K in all cases.

6.1 Organic Compounds as the Electrode of Rechargeable Batteries

The discovery of conducting doped conjugated polymers, such as polypyrrole and polyaniline, in the 1980's emerges as a new possibility for the application as an electrode of rechargeable batteries. These compounds exhibit low solubility due to the large mass and disperse utilization of conductive additives owed to their high electron conductivity. However, drawbacks such as low capacities, low stability of the charged phase and fast self-discharge produced the fail of these materials in the application as electrode of secondary batteries.

A different way of taking advantage of the great features shown by the conjugated polymers is to anchor on them high capacity redox functional groups. This method can produce high capacity systems since the attached redox groups can store extra charge avoiding issues related to the stability of the polymer backbone. Moreover, it ensures the required low solubility of the molecules. This strategy is schematically represented in Figure 6.2 where the first electron reduction (green color) ends up on the polymer backbone providing the required conductivity of the system. Then, the second electron reduction (red color) is stored on the active redox center molecule. However, the anchoring of the redox centers on the polymer backbone is constrained by the redox matching between the backbone and the redox group. Moreover, the potential window is restricted by the stability of the polymer backbone. Therefore, it is important to investigate compositions, backbones plus high capacity molecules, that can show energetic match.

This investigation was divided into two parts: Firstly, a framework to compute the reduction potential of conjugated polymers was developed on the basis of the density functional theory and reaction field method, Sec. 6.2. In sequence, strategies to tune the reduction potential of small molecules, that could serve as an electro-active center on polymers backbone, were derived in Sec. 6.3.

6.2 Case 01: Assessing Electrochemical Properties of conjugated polymers

It is well known that conjugated polymers such as polypyridine (PPY) and as polythiophene are good electronic conductors under doping conditions. This important feature of these conjugated polymers rendered applications in many areas with the focus on light-emitting diodes and solar cells [92, 93]. However, the high electronic transport properties of these materials could also serve in applications concerning to energy storage, more specifically, in applications as an electrode of rechargeable batteries. Most of the theoretical works for the target compounds, polypyridine and polythiophene, have their focus on the investigation of electronic transitions associated with photo-excitation effects.

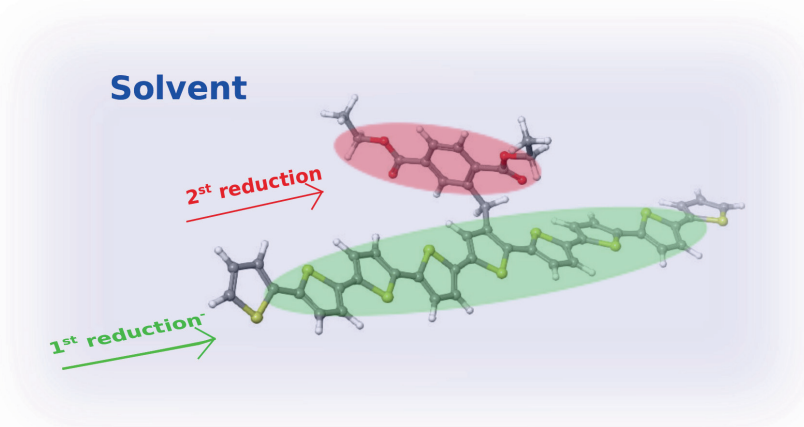


Figure 6.2. Polymer backbone with a redox active center molecule anchored on. In green color, one can see the first electron reduction with the extra electron ending on the backbone. Then, the conductivity of the conjugated polymer is warranted. In red one can observe the second electron reduction going to the anchored molecule. The redox reaction takes place in a solvent medium represented by blue color.

Here, the electrochemical properties of the PPY and polythiophene in solution are studied within the developed first-principles based computational protocol. Moreover, the main predicted results were tested against the experimental measurements.

The idea behind the developed framework is to predict the reduction potential of conjugated polymers in solution. The evolution of the oligomers' properties with increasing chain length gives us the possibility to estimate the reduction potential of the target polymer through an extrapolation to an infinite chain. This approach has been successfully applied to investigate electronic transition in PPY, for example [94, 95]. For each considered oligomer, first principles calculations, based on the density functional theory and the reaction field method, were performed to evaluate redox potentials in solution by applying the 6-311G** basis set [96, 97] and the hybrid functional B3LYP [98–100].

Figure 6.3 (a) shows the computed reduction potential vs. Fc^0/Fc^+ for polythiophene in acetonitrile against the number of monomers in the oligomers (n). An ordinary least squared (OLS) estimation of the simple linear model was performed and the following linear relation comes up $E^0 = -1.81 + 2.0877 \times (1/n)$. This relation provides the tools to predict the redox potential of an infinite chain, $n \rightarrow \infty$ or $1/n \rightarrow 0$, where the predicted potential is -1.81 V vs.

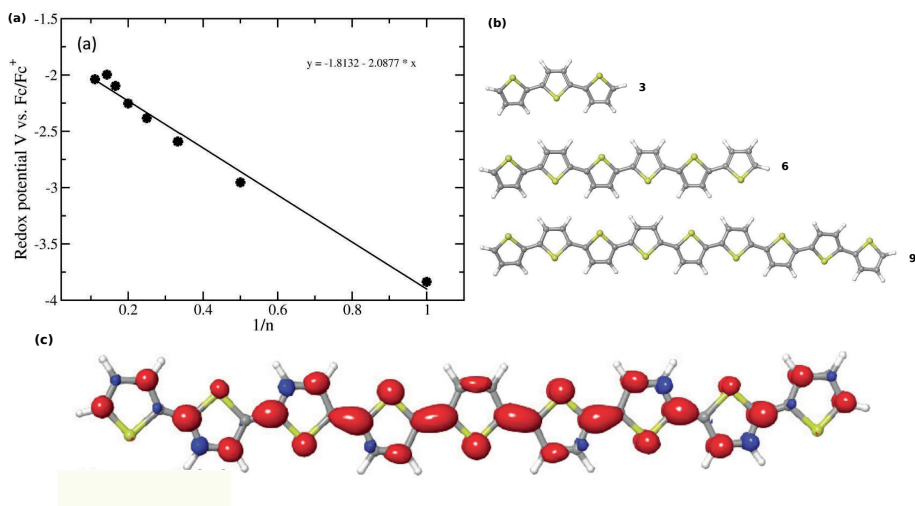


Figure 6.3. (a) Reduction potential as a function of the inverse of the oligomer length in acetonitrile solvent. (b) Picture representing the oligomers with $n=3, 5$ and 9 . (c) Spin density picture of the doped oligomer with $n=9$ and molecular net charge -1 .

Fc^0/Fc^+ for polythiophene. The voltammetric response from polythiophene films on glassy carbon electrodes showed n-doping starting close to -1.70 V in fair agreement with the -1.81 V computed here.

The variation of the predicted redox potential with the chain length seems to converge rather quickly presenting a difference of only 200 mV when comparing the infinite chain extrapolation and the evaluated value for the oligomer with 7 monomers. This effect may be due to the polaron length that is formed during the polymer reduction. Figure 6.3 (c) presents the spin density of the reduced state in the oligomer with $n=9$. As observed, the extra charge in this compound is mainly concentrated on the central seven units of the oligomer creating distortions that stabilize the formation of the electron polaron defect. Moreover, most of the charge gets localized in the bonds between the rings. As it is evidenced, the reduction process ends up with an increased double bond character in the bonds linking the rings of the charged state oligomer. The energetic compensation due to the bonds distortion with the polaron formation amounts to 0.13 eV.

A similar relation is derived for PPY. In this case, the predicted reduction potential goes to -2.13 V vs. Fc^0/Fc^+ which is 300 meV lower than the polythiophene case. The energetic compensation due to the lattice distortion in the PPY amounts to 0.07 eV stabilizing the formation of the bond distortions in the charged state. The extension of the electron polaron is roughly estimated to cover 6 to 7 units for the PPY.

The same kind of analysis was performed for the band gap of PPY and polythiophene. Owing to the linear relationship of the band gap against $1/n$, an extrapolation to an infinity chain provides us with the optical band gap of both compounds, 1.94 eV and 2.88 eV for polythiophene and PPY, respectively. These values were in good agreement with the experimental results, 2.0 eV and 2.9 eV, respectively, revealing the power of the proposed protocol.

In summary, a theoretical approach combining the reaction field method and density functional theory was developed to analyze the evolution of the electrochemical properties of solvated oligomers. The polymer properties are then estimated from intercept coefficients of OLS regressions on simple linear models. The predicted properties display good agreement with the experimental measures. The fair agreement confirms the power of the proposed protocol. Now, it can be extended to other compounds in order to identify new materials with superior properties for application in electrodes of organic rechargeable batteries.

6.3 Case 02: Designing Strategies to Tune Reduction Potential of Organic Molecules

This part of the investigation aims to design strategies to tune the reduction potential of small molecules working as promising candidates for the application as redox centers on conjugated polymers. As explained above, the anchoring of the small molecules on the polymer backbone is constrained by the redox matching between the backbone and the redox group together with the polymer stability window. Therefore, it is crucial to identify strategies to tune the redox potential of possible candidates for such application. To do this job, the framework of density functional theory connected with the reaction field method has been applied to predict the formal potential of 137 molecules and to identify promising candidates for the referent application. The effects of including different ring types, e.g. fused rings or bonded rings, heteroatoms, π bonds, as well as carboxyl groups on the formal potential, have been rationalized. Finally, we have identified a number of molecules with acceptable theoretical capacities that show redox matching with thiophene-based conducting polymers which, hence, are suggested as pendant groups for the development of conducting redox polymer based electrode materials.

The evaluation of the redox potentials was performed within the density functional theory as implemented in the Jaguar software [90, 91]. The hybrid functional B3LYP [98–100] was employed to treat the exchange and correlation term in the Koh-Sham Hamiltonian together with the 6-311G** basis set [96, 97]. The accuracy of the theoretical method has been assessed through the correlation between the experimental data and the predicted reduction potential of 8 molecules as shown in Figure 6.4. The slope and intercept coefficients in the linear regression are 0.99 and 0.20, for the first reduction, and 1.10 and

0.97, for the second reduction. The evaluation of the R^2 allows one to have an idea of the goodness of the linear fitting. In this case, the first reduction reaction showed R^2 equal to 0.99 indicating the high accuracy of the proposed theory level. Finally, all reported redox potentials were corrected by the linear fitting emerged from the correlation of the predicted potentials and measured values.

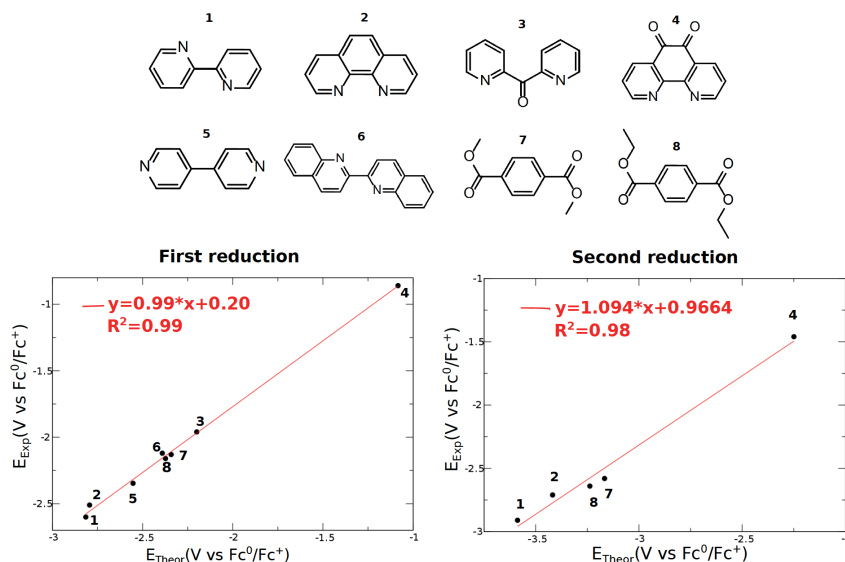


Figure 6.4. Set of molecules used to produce the correlation between the experimental reduction potential and the predicted value within the specified level of theory.

After the investigation of the reduction potential of the 137 molecules, the following trends were identified:

1. It is shown that molecules with same molecular formula but presenting different geometries can produce distinct redox values. This is due to the electronic delocalization. The one with the higher degree of electronic delocalization (greater conjugation) presents higher reduction potential.
2. The fusion of phenyl groups with another 6C ring results in higher potential than the case where a 5C ring is fused with the 6C ring.
3. The inclusion of O atoms, as carbonyl groups, can produce greater potentials. Moreover, if more than one O is added, then the relative position between them becomes important for the produced potential shift.
4. The substitution of NH on top of aliphatic groups, CH_2 , in the 5C ring compounds induces lower reduction potentials.
5. Compounds containing carbonyl groups tend to minimize the effects of substitution.

6. The inclusion of O and S as heteroatoms on the five membered rings usually induces values similar to the one found for the non-substituted compound. Moreover, it is observed that NH substitution induces lower potentials than O and O induces lower potential than S addition, with O and S substitution showing a very small difference in the first reduction potential. Finally, the first and second electron separation reveal lower values in the compounds with S as compared to compounds containing substituted O.
7. It is inferred that the inclusion of new C=C, and hence an extended conjugated system results in more reactive systems and, as a consequence, higher potentials are observed. On the other hand, the inclusion of phenyl groups generally produces downshift of the reduction potential.

The shift in the reduction potential revealed by the molecular design with the above features is linked to changes on the frontier molecular orbitals (HOMO and LUMO) over structural modifications. The process of reduction is essentially an injection of electrons in the LUMO orbitals. Therefore, molecules with higher LUMO energy can easily accept electrons being the main reason to the predicted lower reduction potential values. On the other hand, a lower LUMO orbital is one of the triggering factors for higher reduction potentials. Figure 6.5 presents the linear correlation of the predicted potential and the LUMO orbital of the 137 investigated molecules. A R^2 of 0.99 is obtained confirming the great correlation between these two quantities and supporting the concept discussed above.

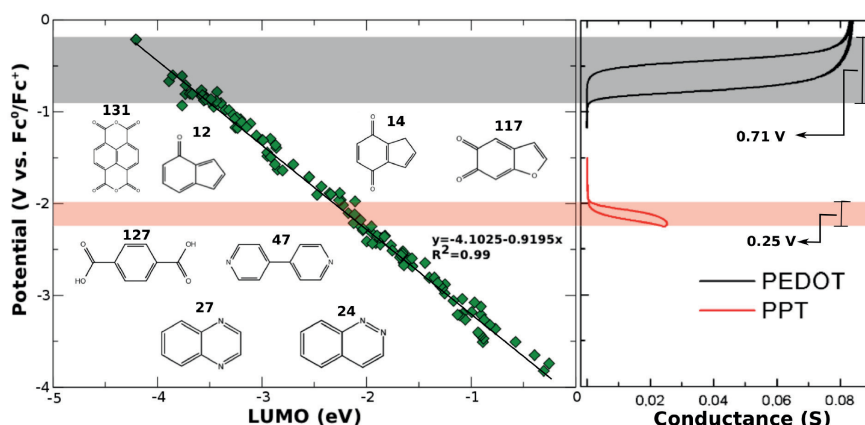


Figure 6.5. Left side: Correlation between LUMO (eV) and the predicted reduction potentials (V) for all molecules considered in this work. Right side: Conductance of the polyphenylthiophene (PPT) and PEDOT obtained as explained in Ref. [102]

Figure 6.5 also displays the reversely p-doped potential window varying from -0.19 V to -0.90 V vs. Fc^0/Fc^+ for the PEDOT backbone as well as the n-doping potential window ranging from -1.99 V to -2.24 V vs. Fc^0/Fc^+ for the Polyphenylthiophene (PPT) as reported by L. Yang et al. [102]. For the PDOT case, 25 molecules among the 137 investigated have presented energy matching with the backbone. From the 25 molecules with energy matching, 4 of them were chosen as the best candidates owing to their greater delivered theoretical capacities reaching values up to 206.09 mA/g. These molecules are drawn in the up part of Figure 6.5. For the PPT case, 12 molecules with the first reduction potential inside the constrained region were found. Again, four molecules were selected as the best candidates based on the greater delivered theoretical capacities. These compounds are depicted on the down part of Figure 6.5

In summary, many strategies to tune the reduction potential of molecules were rationalized with the primer goal of creating receipts able to shift the delivered redox potential of such compounds. The LUMO change under the design strategies appears as the main responsible for the potential shift. Moreover, many molecules were identified as promising candidates for the application as redox centers connected with polyphenylthiophene and PEDOT as the backbone.

7. Summary

In this thesis, the framework of the density functional theory has been employed together with other theoretical tools to study properties such as ionic diffusion, redox potential, electronic structure and crystal structure prediction. The primary goal is to use these tools to model new materials with relevance to electrode application for the next generation of rechargeable batteries. The thesis is divided into six chapters: The first deals with the general problem of materials for electrode application. Then, the theoretical background concerning the density functional theory is described in chapter two. The third chapter is devoted to describe the applied tools to investigate transport properties. Among them, the formalism of ab initio molecular dynamics and transition state theory are presented. In sequence, the employed methods to predict crystal structures and how they are used to compute ionic insertion potentials are shown in chapter 4. Chapter 5 makes links between the material's electronic structure and specific properties of importance as electrode. Finally, a description of how to compute redox potentials in a solution is presented.

Along chapter three, many different properties related to transport of defects have been presented. The framework of the density functional theory based on the hybrid functional approach and the nudged elastic band method were used to study the mobility of charge carriers and intrinsic defects in Na_2O_2 . It was shown that the charge transport in sodium peroxide would mainly occur through the diffusion of hole polarons. The influence of the Hubbard term and the crystal structures of LiFeSiO_4 in the ionic diffusion mechanisms were investigated. Generally speaking, the inclusion of the U term in the Kohn-Sham Hamiltonian leads to lower activation barriers than in the case where the barriers are computed with pure GGA. Owing to the alternative alignment of the FeO_4 tetrahedral in LiFeSiO_4 , Li^+ ions must migrate in a sort of zig-zag diffusion in the monoclinic silicate while the orthorhombic structure, with aligned FeO_4 tetrahedral, must likely have ions following a straight line diffusion. Ionic diffusion mechanisms were elucidated for the cathode materials $\text{Na}_{2.5}\text{Mn}_{1.75}(\text{SO}_4)_3$ and $\text{Na}_2\text{Fe}_2(\text{SO}_4)_2$ as well.

Chapter four is dedicated to study the ionic insertion reaction in some host compounds. The fractional coordinates of Na atoms into $\text{NaFe}_2(\text{SO}_4)_2$, forming $\text{Na}_2\text{Fe}_2(\text{SO}_4)_2$, were revealed by employing the basin hopping algorithm. We have also replaced the Fe atoms by some other transition metals to study the possibility of a compound showing greater specific energy. This strategy allows us to predict the vanadium based compound, $\text{NaV}_2(\text{SO}_4)_2$, as a good alternative to $\text{NaFe}_2(\text{SO}_4)_2$. Subsequently, the evolutionary algorithm was used

to study chloranil molecules as a new organic candidate for a cathode of Na batteries. This work aimed to reveal the driving forces behind the structural changes of $C_6Cl_4O_2$ during the battery reaction (ionic insertion). We were able to point out the main entity responsible for the structural change and also the lower specific capacity obtained in the experiment in comparison to the theoretical specific capacity. Moreover, we showed that this method can bring out reasonable results concerning the ionic insertion potential. The main trends regarding the application of the 2D compounds, B_2H_2 and Si_2BN , as an anode of advanced rechargeable batteries were investigated. The application of the swamping basin hopping algorithm helped to access the ground state structures for each ionic concentration. Once these structures were available, we have derived the insertion potential profile and investigated the ionic diffusion mechanisms for both materials. We have also compared the computed properties with the value revealed by other 2D materials employed as the anode of a rechargeable battery.

The investigation of ionic insertion in $Nb_2O_2F_3$ is discussed in Chapter 5. We have revealed that the extra electrons donated by Li^+ ions are reducing π^2 molecular states of the Nb–Nb. For the case of $Na_2M_2(SO_4)_3$ ($M=Fe, Mn, Co$ and Ni), we revealed that the compounds with Co and Ni come with great participation of the oxygen sublattice in the redox reaction. It accounts for the lower predicted volume change in these compounds.

Finally, the employed method to predict redox potential in solution is presented together with two main applications. Firstly, we have presented a theoretical framework to estimate the redox potential of conjugated polymers in solution. The idea was to use the evolution of the oligomer's properties with increasing chain length to estimate the reduction potential of the target polymer through an extrapolation to an infinite chain. The redox potential of two polymers, PPY and polythiophene, were computed and compared with the experimental value. The fair agreement confirms the power of the proposed protocol. The second part of this chapter was devoted to designing strategies to tune the reduction potential of small molecules working as promising candidates for the application as redox centers on conjugated polymers.

Great development has been achieved in the field of advanced rechargeable batteries during the last decade with the discovery of new materials with superior performance. However, many fundamental points are still unclear or not fully understood. In this context, this thesis showed how first principles calculations can contribute to the investigation of a number of properties related to materials with relevance for electrodes of rechargeable batteries. It ultimately supports new accomplishments in the area with the production of batteries with higher capacity, lower prices and environmentally friendly.

8. Sammanfattning

I den här avhandlingen har ramverket från täthetsfunktionalteorin använts tillsammans med andra teoretiska verktyg för att studera egenskaper som jondiffusion, reduktionspotential, elektronstruktur och kristallstruktur. Det primära målet är att använda dessa verktyg för att modellera nya material relevanta för elektroder i nästa generations uppladdningsbara batterier. Avhandlingen är uppdelad i sex kapitel. Det första beskriver generella problem hos material som kan användas som elektroder. Sedan beskrivs, i kapitell två den teoretiska bakgrunden rörande täthetsfunktionalteorin. Det tredje kapitlet avser beskriva verktygen som använts för att undersöka transportegenskaper, bland dem formalismen av ab-initio molekylärdynamik och teorin om övergångsfaser. Sedan beskrivs metoder för att förutsäga kristallstrukturer och hur de använts för att beräkna potentialen vid insättning av joner i kapitel fyra. Kapitel fem länkar ihop ett materials elektronstruktur med särskilda egenskaper av vikt för elektroder. Slutligen presenteras beskrivningen om hur man beräknar reduktionspotentialer i en lösning.

Inom kapitel tre undersöks många olika egenskaper relaterade till transport av defekter. Ramverket från täthetsfunktionalteorin med användning av hybridfunktionalteori och ”nudged elastic band”-metoden användes för att studera mobiliteten hos laddningsbärare och inneboende defekter i Na_2O_2 . Det visade sig att laddningstransporten i natriumperoxid till största delen sker genom diffusion av hålpolaroner. Inverkan av Hubbardtermen (U-termen) och kristallstrukturen hos LiFeSiO_4 på jondiffusionsmekanismerna undersöktes. Generellt leder tillägget av U-termen i Kohn-Sham-Hamiltonianen till lägre aktiveringsbarriärer än i fallet där barriärerna beräknas med endast GGA. På grund av de alternativa arrangeringarna av FeO_4 -tetraedern i LiFeSiO_4 måste Li^+ joner migrera i en form av sicksacksdiffusion i det monokliniska systemet, men i det ortorombiska systemet följa en rät linje. Slutligen förklarades jondiffusionsmekanismerna för katodmaterialen, $\text{Na}_{2.5}\text{Mn}_{1.75}(\text{SO}_4)_3$ och $\text{Na}_2\text{Fe}_2(\text{SO}_4)_2$.

I kapitell fyra studeras joninförningsreaktioner i några värdföreningar. Koordinaterna för insättning av Na-atomer $\text{NaFe}_2(\text{SO}_4)_2$ för att bilda $\text{Na}_2\text{Fe}_2(\text{SO}_4)_2$ tog fram genom att använda basin hoppingd-algoritmen. Vi har också ersatt Fe-atomerna med några andra övergångsmetaller för att studera möjligheten att komma fram till en förening med större specifik energi. Den här strategin låter oss uppskatta den vanadinbaserade föreningen, $\text{NaV}_2(\text{SO}_4)_2$, som ett bra alternativ till $\text{NaFe}_2(\text{SO}_4)_2$. Sedan användes den utvecklande algoritmen för att studera klorinnehållande molekyler som en ny organisk katodkandidat i Na-batterier. Arbetet fokuserar på att visa drivkraften bakom

strukturella förändringar av $C_6Cl_4O_2$ under batterireaktionen (joninförning). Vi kunde peka ut den huvudsakliga orsaken för den strukturella förändringen, men också den lägre specifika kapaciteten funnen i experiment i jämförelse med den teoretiska specifika kapaciteten. Dessutom visade vi att den här metoden kan ge oss godtagbara resultat rörande joninförningspotentialen. Slutligen undersöktes de huvudsakliga tillvägagångssätten gällande användning av 2D-material, B_2H_2 och Si_2BN , som anoder i avancerade uppladdningsbara batterier. Användandet av basin hopping-algoritmen hjälpte oss att få tillgång till grundnivåstrukturerna för varje jonkoncentration. När strukturerna var kända, härledde vi utseendet av införningspotentialen och undersökte jondiffusionsmekanismen för båda materialen. Slutligen jämförde vi de beräknade storheterna med värdena för andra 2D-material använda som anoder i uppladdningsbara batterier.

Undersökningen av joninförning i $Nb_2O_2F_3$ diskuteras i kapitel fem. Vi har visat att de extra elektronerna donerade av Li^+ jonerna reducerar π^2 molekylnivåer hos Nb-Nb. I fallet $Na_2M_2(SO_4)_3$ ($M=Fe, Mn, Co$ och Ni) visade vi att i föreningarna med Co och Ni deltog syredelen av gittret bra i reduktionsreaktionen. Det här är den huvudsakliga orsaken till den lägre uppskattade volymförändringen i de föreningarna.

Slutligen presenteras den använda metoden för att beräkna reduktionspotentialen i en lösning tillsammans med två huvudsakliga användningsområden. Till att börja med presenterade vi ett teoretiskt ramverk för att uppskatta reduktionspotentialen för polymerer i en lösning. Idén var att använda utvecklingen av egenskaperna hos delsegmenten, med ökande kedjelängd, för att uppskatta reduktionspotentialen hos den tänkta polymeren genom extrapolation till en oändlig kedja. Reduktionspotentialen hos två polymerer, PPY och polytiofen, beräknades och jämfördes med de experimentella värdena. Den lovande överensstämmelsen styrker kraften hos det föreslagna regelverket. Den andra delen av det här kapitlet avser att designa strategier för att fininställa reduktionspotentialen hos små molekyler, som kandidater för reduktionscentra i polymerer.

Den här avhandlingen visar hur första-principberäkningar kan bidra till undersökningen av många olika egenskaper relaterade till material relevanta som elektroder i uppladdningsbara batterier. Det här området har utvecklats mycket under det senaste årtiondet. Fortfarande återstår många fundamentala punkter som är oklara eller inte helt förstådda. Användandet av kvantmekaniska beräkningar tillsammans med experiment verkar vara en bra strategi för att fylla de här kunskapsluckorna. Det här kommer under kommande år att leda till produktion av batterier med högre kapacitet, lägre pris och som dessutom är miljövänliga.

9. Acknowledgments

I would like to take this opportunity to express my gratitude to many people who contributed to the elaboration of this work. Firstly, I would like to thank my supervisor Rajeev Ahuja for having accepted me as a Ph.D. student in his group. He also brought to me a collection of very interesting problems together with a research freedom that encouraged my independence as a researcher. I thank Moyses Araújo who always discuss physics with me bringing different perspectives into the projects. Thanks to Martin Sjödin for the fruitful collaboration and all discussions concerning the organic batteries projects.

Special thanks to all members of our research group for providing me with a great work environment full of exiting scientific discussions. For translating the summary of this thesis into Swedish I would like to thank Emil Edin and John Wörnå. I specially thank Amitava Banerjee, Vivekanand Shukla, Naresh Jena, John Wörnå, Teeraphat Watcharatharapong and Sudip Chakraborty for the very fruitful collaboration and for all scientific discussions. Another thanks goes to Rodrigo Amorim for the helpful discussions regarding my projects. I have really enjoyed working with you all and I hope we continue collaborating in future projects.

I believe that most of the work I have done here at Uppsala University were strongly influenced by the people who advised me before I have arrived in Sweden. For that, I thank Antonio Ferreira, Jailton Almeida and Ralph Sheicher for advising me during my master thesis in Brazil. I also thank Manuel Pereiro and Daniel Baldomir for advising me in the master thesis I did in Spain.

Many thanks to John, Emil, Amitava, Jenny, Moyses, Giane, Cleber, Vivek and Naresh for having read the thesis and point out topics that enhanced the quality of the work. I am also thankful to everybody in the Materials theory division. You all gave me the chance of participating in an alive scientific environment with talks and *fikas*.

Agradeço também a toda minha família que, de todas as formas, me ajudou a realizar este sonho, do fundo do meu coração obrigado a todos. Además, estoy muy agradecido de mi esposa, Jenny, por toda la paciencia que tuvo todo este tiempo, por ayudarme y motivarme en los momentos más difíciles en la producción de este trabajo, gracias mi amor.

References

- [1] International energy outlook. <http://www.worldenergyoutlook.org> (International Energy Agency, 2011).
- [2] S. Chu and A. Majumdar. Opportunities and challenges for a sustainable energy future. *Nature*, 488:294–303, 2012.
- [3] D. Larcher and JM. Tarascon. Towards greener and more sustainable batteries for electrical energy storage. *Nature Chemistry*, 7:19–29, 2015.
- [4] T. Nagaura and K. Tozawa. Lithium ion rechargeable battery. *Prog. Batteries Solar Cells*, 9:209, 1990.
- [5] K. Mizushima, P. C. Jones, P. J. Wiseman, and J. B. Goodenough. Li_xCoO_2 ($0 < x < 1$): A new cathode material for batteries of high energy density. *Materials Research Bulletin*, 15:783, 1980.
- [6] R. Yazami and P. Touzain. A reversible graphite-lithium negative electrode for electrochemical generators. *Journal of Power Sources*, 9.3:365, 1983.
- [7] P. Bruce, S. Freunberger, L. Hardwick, and JM. Tarascon. Li-O₂ and Li-S batteries with high energy storage. *Nat. Mater.*, 11:19–30, 2012.
- [8] Z. P. Song and H. S. Zhou. Towards sustainable and versatile energy storage devices: an overview of organic electrode materials. *Energ. Environ. Sci.*, 6: 2280, 2013.
- [9] D. L. Williams, JJ Byrne, and J. S. Driscoll. A high energy density lithium/dichloroisocyanuric acid battery system. *J. Electrochem. Soc.*, 116:2, 1969.
- [10] H. Alt, H. Binder, A. Köhling, and G. Sandstedt. Investigation into the use of quinone compounds-for battery cathodes. *J. Electrochem. Soc.*, 17:873, 1972.
- [11] Y. L. Liang, z. L. Tao, and J. Chen. Organic electrode materials for rechargeable lithium batteries. *Advanced Energy Materials*, 2:742, 2012.
- [12] H. Chen, M. Armand, G. Demailly, F. Dolhem, P. Poizot, and JM. Tarascon. From biomass to a renewable $\text{Li}_x\text{C}_6\text{O}_6$ organic electrode for sustainable li-ion batteries. *ChemSusChem*, 1:348, 2008.
- [13] H. Chen, M. Armand, M. Courty, M. Jiang, C. P. Grey, F. Dolhem, and JM. Tarascon. Lithium salt of tetrahydroxybenzoquinone: Toward the development of a sustainable Li-ion battery. *J. Am. Chem. Soc.*, 131:8984, 2009.
- [14] H. Kim, J. Hong, K. Park, H. Kim, S. Kim, and K. Kang. Aqueous rechargeable Li and Na ion batteries. *Chem. Rev.*, 23:11788, 2014.
- [15] P. Hartmann, C. L. Bender, M. Vračar, J. Janek A. K. Drür, A. Garsuch, and P. A. Adelhelm. A rechargeable room-temperature sodium superoxide (NaO_2) battery. *Nat. Mater.*, 12:228–2320, 2013.
- [16] B. D. McCloskey, A. Valery, A. C. Luntz, S. R. Gowda, G. M. Wallra, J. M. Garcia, T. Mori, and L. E. Krupp. Combining accurate O₂ and Li₂O₂ assays to separate discharge and charge stability limitations in nonaqueous Li-O₂ batteries. *J. Phys. Chem. Lett.*, 4:2989, 2013.

- [17] S. A. Freunberger, Y. Chen, N. E. Drewett, L. J. Hardwick, F. Bardé, and P. G. Bruce. The lithium- oxygen battery with ether-based electrolytes. *Angew. Chem. Int. Ed. Engl.*, 50:8609, 2011.
- [18] V. Viswanathan, K. S. Thygesen, J. S. Hummelshøj, J. K. Nørskov, G. Girishkumar, B. D. McCloskey, and A. C. Luntz. Electrical conductivity in Li_2O_2 and its role in determining capacity limitations in non-aqueous Li- O_2 batteries. *J. Chem. Phys.*, 135:214704, 2011.
- [19] A. C. Luntz, V. Viswanathan, J. Voss, J. B. Varley, and A. Speidel. Tunneling and polaron charge transport through Li_2O_2 in Li- O_2 batteries. *J. Phys. Chem. Lett.*, 50:3494, 2013.
- [20] J. M. Garcia-Lastra, J. S. G. Myrdal, R. Christensen, K. S. Thygesen, and T. Vegge. DFT+U study of polaronic conduction in Li_2O_2 and Li_2CO_3 : Implications for li-air batteries. *J. Phys. Chem. C*, 5568-5577:117, 2013.
- [21] M. D. Radin and D. J. Siegel. Charge transport in lithium peroxide: Relevance for rechargeable metal-air batteries. *Energy Environ. Sci.*, 6:2370-2379, 2013.
- [22] P. Albertus, G. Girishkumar, B. McCloskey, R. S. Sánchez-Carrera, B. Kozinsky, J. Christensen, and A. C. Luntz. Identifying capacity limitations in the Li/oxygen battery using experiments and modeling. *J. Electrochem. Soc.*, 158:A343, 2011.
- [23] N. Imanishi, A. C. Luntz, and P. Bruce. *The Lithium Air Battery: Fundamentals*. Springer Science Business Media, 2014. ISBN 0.
- [24] P. Hohenberg and W. Kohn. Inhomogeneous electron gas. *Phys. Rev.*, 136: B864-B871, 1964.
- [25] W. Kohn and L. J. Sham. Self-consistent equations including exchange and correlation effects. *Phys. Rev.*, 140:A1133-A1138, 1965.
- [26] R. G. Parr and W. Yang. *Density-functional theory of atoms and molecules*. Oxford University Press, 1989. ISBN 0.
- [27] A. D. Becke. Density-functional exchange-energy approximation with correct asymptotic behavior. *Phys. Rev. A*, 38:3098-3100, 1988.
- [28] J. P. Perdew and Y. Wang. Accurate and simple analytic representation of the electron-gas correlation energy. *Phys. Rev. B*, 45:13244, 1992.
- [29] J. P. Perdew, K. Burke, and M. Ernzerhof. Generalized gradient approximation made simple. *Phys. Rev. Lett*, 77:3865, 1996.
- [30] J. Klimes and A. Michaelides. Perspective:advances and challenges in treating van der waals dispersion forces in density functional theory. *J. Chem. Phys.*, 137:120901, 2012.
- [31] R. M. Martin. *Electronic Structure: Basic Theory and Practical Methods*, volume 28. Cambridge University Press, 2004. ISBN 978-3-540-08705-2.
- [32] P. Mori-Sánchez, A. Cohen, and W. Yang. Localization and delocalization errors in density functional theory and implications for band-gap prediction. *Phys. Rev. Lett*, 100:146401, 2008.
- [33] A. J. Cohen, P. Mori-Sánchez, and W. Yang. Insights into current limitations of density functional theory. *Science*, 321:792-794, 2008.
- [34] G. I. Csonka and B. C. Johnson. Inclusion of exact exchange for self-interaction corrected H3 density functional potential energy surface. *Theoretical Chemistry Accounts*, 99:158, 1998.

- [35] A. I. Liechtenstein, V. I. Anisimov, and J. Zaane. Density-functional theory and strong interactions: Orbital ordering in Mott-Hubbard insulators. *Phys. Rev. B*, 52:R5467, 1995.
- [36] S. Y. Savrasov C. J. Humphreys S. L. Dudarev, G. A. Botton and A. P. Sutton. Electron-energy-loss spectra and the structural stability of nickel oxide: An LSDA+ U study. *Phys. Rev. B*, 57:1505, 1998.
- [37] J. Heyd, G. E. Scuseria, and M. Ernzerhof. Hybrid functionals based on a screened coulomb potential. *J. Chem. Phys.*, 118:8207, 2003.
- [38] J. F. Dobson and T. Gould. Calculation of dispersion energies. *J. Phys. Condens. Matter*, 24:073201, 2012.
- [39] S. Grimme. Accurate description of van der waals complexes by density functional theory including empirical corrections. *J. Comput. Chem.*, 25:1463, 2004.
- [40] S. Grimme. Semiempirical GGA-type density functional constructed with a long-range dispersion correction. *J. Comput. Chem.*, 27:1787, 2006.
- [41] S. Grimme, J. Antony, S. Ehrlich, and H. Krieg. A consistent and accurate ab initio parametrization of density functional dispersion correction (DFT-D) for the 94 elements H-Pu. *J. Comput. Chem.*, 32:154104, 2010.
- [42] A. Tkatchenko and M. Scheffler. Accurate molecular van der waals interactions from ground-state electron density and free-atom reference data. *Phys. Rev. Lett.*, 102:073005, 2009.
- [43] J. F. Dobson and T. Gould. Exchange-hole dipole moment and the dispersion interaction. *J. Chem. Phys.*, 123:154104, 2005.
- [44] A. Szabo and N. S. Ostlund. *Modern Quantum Chemistry: Introduction to Advanced Electronic Structure Theory*. McGraw-Hill.
- [45] P. E. Blöchl. Projector augmented-wave method. *Phys. Rev. B*, 50: 17953–17979, 1994.
- [46] D. R. Hamann, M. Schlüter, and C. Chiang. Norm-conserving pseudopotentials. *Phys. Rev. Lett.*, 43:1494–1497, 1979.
- [47] H. J. Berendsen, J. V. Postma, W. F. van Gunsteren, A. R. H. J. Dinola, and J. R. Haak. Molecular dynamics with coupling to an external bath. *Journal of chemical physics*, 81:3684, 1984.
- [48] S. Nosé. A unified formulation of the constant temperature molecular dynamics methods. *The journal of chemical physics*, 81:511, 1984.
- [49] W. G. Hoover. Canonical dynamics: Equilibrium phase-space distributions. *Physical review A*, 31:1695, 1985.
- [50] H. Jónsson, G. Mills, and K. W. Jacobsen. *Nudged Elastic Band Method for Finding Minimum Energy Paths of Transitions, in Classical and Quantum Dynamics in Condensed Phase Simulations*. World Scientific, 1998.
- [51] A. Nyttén, A. Abouimrane, M. Armand, T. Gustafsson, and J.O. Thomas. Electrochemical performance of $\text{Li}_2\text{FeSiO}_4$ as a new Li-battery cathode material. *Electrochem. Commun.*, 7:156, 2005.
- [52] S. Nishimura, S. Hayase, R. Kanno, M. Yashima, N. Nakayama, and A. Yamada. Structure of $\text{Li}_2\text{FeSiO}_4$. *J. Am. Chem. Soc.*, 130:13212, 2008.
- [53] M.E. Arroyo de Dompablo, M. Armand, JM. Tarascon, and U. Amador. On-demand design of polyoxianionic cathode materials based on electronegativity correlations: an exploration of the Li_2MSiO_4 system (M= Fe,

- Mn, Co, Ni). *Electrochem. Commun.*, 8:1292, 2006.
- [54] S. Q. Wu, Z. Z. Zhu, Y. Yang, and Z. F. Hou. Structural stabilities, electronic structures and lithium deintercalation in Li_2MSiO_4 system (M= Fe, Mn, Co, Ni): A GGA and GGA+U study. *Electrochem. Commun.*, 8:1243, 2006.
- [55] D. Dwibedi, R. B. Araujo, S. Chakraborty, P. Shanbogh, N. Sundaram, R. Ahuja, and P. Barpanda. $\text{Na}_{2.44}\text{Mn}_{1.79}(\text{SO}_4)_3$: a new member of the alluaudite family of insertion compounds for sodium ion batteries. *J. Mater. Chem. A*, 3:18564, 2015.
- [56] G. K. P. Dathar, D. Sheppard, K. J. Stevenson, and G. Henkelman. Calculations of Li-ion diffusion in olivine phosphates. *Chem. Mater.*, 23:4032, 2011.
- [57] K. Hoang and M. Johannes. Tailoring native defects in LiFePO_4 : Insights from first-principles calculations. *Chem. Mater.*, 23:3003, 2011.
- [58] G Makov and MC Payne. Periodic boundary conditions in ab initio calculations. *Physical Review B*, 51(7):4014, 1995.
- [59] M. K. Aydinol, A. F. Kohan, G. Ceder, K. Cho, and J. Joannopoulos. Ab initio study of lithium intercalation in metal oxides and metal dichalcogenides. *Physical review B*, 56:1354, 1997.
- [60] D. J. Wales and J. P. K. Doye. Global optimization by Basin-Hopping and the lowest energy structures of Lennard-Jones clusters containing up to 110 atoms. *J. Phys. Chem. A*, 101:5116, 1997.
- [61] A. R. Oganov and C. W. Glass. Crystal structure prediction using ab initio evolutionary techniques: Principles and applications. *J. Chem. Phys.*, 124: 244704, 2006.
- [62] A. R. Oganov, A. O. Lyakhov, and M. Valle. How evolutionary crystal structure prediction works and why. *Acc. Chem. Res.*, 44:227, 2011.
- [63] Q. Zhu, A. R. Oganov, C. W. Glass, and H. T. Stokes. Constrained evolutionary algorithm for structure prediction of molecular crystals: methodology and applications. *Acta. Crystallogr. Sect. B Struct. Sci.*, 68:215, 2012.
- [64] W. H. Baur and D. Kassner. The perils of cc: comparing the frequencies of falsely assigned space groups with their general population. *Acta Cryst.*, B48: 356, 1992.
- [65] P. Singh, K. Shiva, H. Celio, and J. B. Goodenough. Eldfellite, $\text{NaFe}(\text{SO}_4)_2$: an intercalation cathode host for low-cost na-ion batteries. *Energy and Environmental Science*, 8:3000, 2015.
- [66] H. Kim, J. E. Kwon, B. Lee, J. Hong, M. Lee, S. Y. Park, and K. Kang. High energy organic cathode for sodium rechargeable batteries. *H. Kim, J. E. Kwon, B. Lee, J. Hong, M. Lee, S. Y. Park and K. Kang*, 27:7258, 2015.
- [67] Y. Kubozono, T. Yoshida, H. Maeda, S. Kashino, H. Terauchi, and T. Ishii. X-ray structure analyses of chloranil above and below phase transition temperature. *J. Phys. Chem. Solids*, 58:1375, 1997.
- [68] T. Yamashita, H. Momida, and T. Oguchi. Crystal structure predictions of $\text{Na}_x\text{C}_6\text{O}_6$ for sodium-ion batteries: First-principles calculations with an evolutionary algorithm. *Electrochim. Acta*, 27:1–8, 2016.
- [69] A. Gupta, T. Sakthivel, and S. Seal. Recent development in 2D materials beyond graphene. *Progress in Materials Science*, 73:44–126, 2015.

- [70] A. J. Mannix, X. F. Zhou B. Kiraly, J. D. Wood, D. Alducin, B. D. Myers, X. Liu, B. L. Fisher, U. Santiago, J. R. Guest M. J., and Yacaman A. Ponce A. R. Oganov M. C. Hersam N. P. Guisinger. Synthesis of borophenes: Anisotropic, two-dimensional boron polymorphs. *Sency*, 350(6267):1513, 2016.
- [71] L. C. Xu, A. Du, and L. Kou. Hydrogenated borophene as a stable two-dimensional dirac material with an ultrahigh fermi velocity. *hys. Chem. Chem. Phys.*, 18(39):27284, 2016.
- [72] L. Kou, Y. Ma, C. Tang, Z. Sun, A. Du, and C. Chen. Auxetic and ferroelastic borophane: a novel 2D material with negative Poisson's ratio and switchable dirac transport channels. *Nano letters*, 16(12):7910–7914, 2016.
- [73] V. Nagarajan and R. Chandiramouli. Sensing properties of monolayer borophane nanosheet towards alcohol vapors: A first-principles study. *Journal of Molecular Graphics and Modelling*, 73:208–216, 2017.
- [74] Q. Tang, Z. Zhou, and P. Shen. Are MXenes promising anode materials for Li ion batteries? computational studies on electronic properties and Li storage capability of Ti_3C_2 and $\text{Ti}_3\text{C}_2\text{X}_2$ ($\text{X} = \text{F}, \text{OH}$) monolayer. *Journal of the American Chemical Society*, 134(40):16909–16916, 2012.
- [75] Z. Yang, D. Choi, S. Kerisit, K. M. Rosso, D. Wang, J. Zhang, G. Graff, and J. Liu. Nanostructures and lithium electrochemical reactivity of lithium titanates and titanium oxides: A review. *Journal of Power Sources*, 192(2): 588–598, 2009.
- [76] S. Zhao, W. Kang, and J. Xue. The potential application of phosphorene as an anode material in Li-ion batteries. *Journal of Materials Chemistry A*, 2(44): 19046–19052, 2014.
- [77] M. Mortazavi, C. Wang, J. Deng, V. B. Shenoy, and N. V. Medhekar. Ab initio characterization of layered MoS_2 as anode for sodium-ion batteries. *Journal of Power Sources*, 268:279–286, 2014.
- [78] A. N. Andriotis, E. Richter, and M. Menon. Prediction of a new graphenelike Si_2BN solid. *Physical Review B*, 93(8):081413, 2016.
- [79] H. Chen and M. S. Islam. Lithium extraction mechanism in Li-rich Li_2MnO_3 involving oxygen hole formation and dimerization. *J. Phys. Chem. Solids*, 28: 6656, 2016.
- [80] R. Bader. *Atoms in Molecules: A Quantum Theory*. Oxford University Press, New York.
- [81] E. Sanville, S. Kenny, R. Smith, and G. Henkelman. Improved grid-based algorithm for bader charge allocation. *J. Comput. Chem.*, 28:899, 2007.
- [82] W. Tang, E. Sanville, and G. Henkelman. A grid-based bader analysis algorithm without lattice bias. *J. Phys. Condens. Mat.*, 21:084204, 2009.
- [83] T. T. Tran, M. Gooch, B. Lorenz, A. P. Litvinchuk, M. G. Sorolla II, J. Brgoch, P. C. W. Chu, and A. M. Guloy. $\text{Nb}_2\text{O}_2\text{F}_3$: A reduced niobium (III/IV) oxyfluoride with a complex structural, magnetic, and electronic phase transition. *J. Am. Chem. Soc.*, 137:636, 2015.
- [84] F. Zhou, M. Cococcioni, C. A. Marianetti, D. Morgan, and G. Ceder. First-principles prediction of redox potentials in transition-metal compounds with LDA+U. *Phys. Rev. B*, 70:235121, 2004.

- [85] P. Barpanda, G. Oyama, S. Nishimura, S. Chung, and A. Yamada. A 3.8-v earth-abundant sodium battery electrode. *Natt. Commun.*, 5:4358, 2014.
- [86] J. Tomas, B. Mennucci, and R. Cammi. Quantum mechanical continuum solvation models. *Chem. Rev.*, 105:2999, 2005.
- [87] F. Jensen. *Introduction to Computational Chemistry*. John Wiley Sons Ltd, 4th edition.
- [88] A. D. Bochevarov, E. Harder, T. F. Hughes, J. R. Greenwood, D. A. Braden, D. M. Philipp, D. Rinaldo, M. D. Halls, J. Zhang, and R. A. Friesner. New model for calculation of solvation free energies: Correction of self-consistent reaction field continuum dielectric theory for short-range hydrogen-bonding effects. *J. Phys. Chem.*, 100:11775, 1996.
- [89] D. J. Tannor, B. Marten, R. Murphy, R. A. Friesner, D. Sitkoff, A. Nicholls, M. Ringnalda, W. A. Goddard, and B. Honig. Accurate first principles calculation of molecular charge distributions and solvation energies from ab initio quantum mechanics and continuum dielectric theory. *J. Am. Chem. Soc.*, 116:11875, 1994.
- [90] Jaguar. *Version 8.3, Schrodinger*. New York, Ny, 2018.
- [91] A. D. Bochevarov, E. Harder, T. F. Hughes, J. R. Greenwood, D. A. Braden, D. M. Philipp, D. Rinaldo, M. D. Halls, J. Zhang, and R. A. Friesner. Jaguar: A high-performance quantum chemistry software program with strengths in life and materials sciences. *Int. J. Quantum Chem.*, 113:2101–2142, 2013.
- [92] G. Hughesa and M. R. Bryce. Electron-transporting materials for organic electroluminescent and electrophosphorescent devices. *J. Mater. Chem.*, 15:94, 2015.
- [93] R. Mastria, A. Rizzo, C. Giansante, D. Ballarini, L. Dominici, O. Inganas, and G. Gigli. Role of polymer in hybrid polymer PbS quantum dot solar cells. *The Journal of Physical Chemistry C*, 19:173, 2015.
- [94] J. Gierschner, J. Cornil, and H. J. Egelhaaf. Optical bandgaps of π -conjugated organic materials at the polymer limit: Experiment and theory. *Advanced Materials*, 119:14972, 2007.
- [95] S. Hedström, P. Henriksson, E. Wang, M. R. Andersson, and P. Persson. Light-harvesting capabilities of low band gap donor acceptor polymers. *Phys. Chem. Chem. Phys.*, 16:24853, 2014.
- [96] W. J. Hehre, R. Ditchfield, and J. A. Pople. Self consistent molecular orbital methods. XII. further extensions of gaussian-type basis sets for use in molecular orbital studies of organic molecules. *J. Chem. Phys.*, 56:2257, 1972.
- [97] M. M. Francl, W. J. Pietro, W. J. Hehre, J. S. Binkley, M. S. Gordon, D. J. Defrees, and J. A. Pople. Self consistent molecular orbital methods. XXIII. a polarization type basis set for second-row elements. *J. Chem. Phys.*, 77:3654, 1982.
- [98] D. A. Becke. Density functional exchange energy approximation with correct asymptotic behavior. *Phys. Rev. A*, 38:3098, 1988.
- [99] C. Lee, W. Yang, and R. G. Parr. Development of the Colle-Salvetti correlation-energy formula into a functional of the electron density. *Phys. Rev. B*, 37:785, 1988.
- [100] A. D. Becke. Density functional thermochemistry. III. the role of exact exchange. *J. Chem. Phys.*, 98:5648, 1993.

- [101] K. Kaneto, Y. Kohno, and K. Yoshino. Absorption spectra induced by photoexcitation and electrochemical doping in polythiophene. *Solid state communications*, 51:267, 1984.
- [102] L. Yang, X. Huang, A. Gogolland M. Strømme, and M. Sjödin. Matching diethyl terephthalate with n doped conducting polymers. *J. Phys. Chem. C*, 15: 18956, 2015.
- [103] W. Koch and M. C. Holthausen. *A chemist's guide to density functional theory*. John Wiley Sons Ltd.
- [104] B. Genorio, K. Pirnat, R. Cerc-Korossec, R. Dominko, and M. Gaberscek. Electroactive organic molecules immobilized onto solid nanoparticles as a cathode material for lithium ion batteries. *Angewandte Chemie International Edition*, 49:7222, 2010.
- [105] J. Geng, J. P. Bonnet, S. Renault, F. Dolhem, and P. Poizot. Evaluation of polyketones with N-cyclic structure as electrode material for electrochemical energy storage: case of tetraketopiperazine unit. *Energy Environmental Science*, 3(12):1929, 2010.
- [106] J. P. Perdew, K. Burke, and M. Ernzerhof. Erratum: Generalized gradient approximation made simple. *Phys. Rev. Lett.*, 78:1396, 1997.
- [107] C. Freysoldt, B. Grabowski, T. Hickel, J. Neugebauer, G. Kresse, A. Janotti, and C. G. Van de Walle. First-principles calculations for point defects in solids. *Reviews of Modern Physics*, 86:253, 2014.

Acta Universitatis Upsaliensis

*Digital Comprehensive Summaries of Uppsala Dissertations
from the Faculty of Science and Technology 1584*

Editor: The Dean of the Faculty of Science and Technology

A doctoral dissertation from the Faculty of Science and Technology, Uppsala University, is usually a summary of a number of papers. A few copies of the complete dissertation are kept at major Swedish research libraries, while the summary alone is distributed internationally through the series Digital Comprehensive Summaries of Uppsala Dissertations from the Faculty of Science and Technology. (Prior to January, 2005, the series was published under the title "Comprehensive Summaries of Uppsala Dissertations from the Faculty of Science and Technology".)

Distribution: publications.uu.se
urn:nbn:se:uu:diva-331399



ACTA
UNIVERSITATIS
UPSALIENSIS
UPPSALA
2017